NREL/TP-214-4503 • UC Category: 270 • DE92001172

NREL/TP--214-4503

DE92 001172

The Effectiveness and Stability of Impurity/Defect Interactions and Their Impact on Minority Carrier Lifetime

Annual Subcontract Report
1 August 1990 - 31 July 1991

G. A. Rozgonyi, F. Shimura,
A. Buczkowski, T.-Q. Zhon
North Carolina State University
Raleigh, North Carolina

NREL technical monitor: B. Sopori

National Renewable Energy Laboratory
(formerly the Solar Energy Research Institute)
1617 Cole Boulevard
Golden, Colorado 80401-3393
A Division of Midwest Research Institute
Operated for the U.S. Department of Energy
under Contract No. DE-AC02-83CH10093

Prepared under Subcontract No. XL-8-18097-2

December 1991

On September 16, 1991, the Solar Energy Research Institute was designated a national laboratory, and its name was changed to the National Renewable Energy Laboratory.

NOTICE

Printed in the United States of America
Available from:
National Technical Information Service
U.S. Department of Commerce
5285 Port Royal Road
Springfield, VA 22161

Price: Microfiche A01
Printed Copy A04

Codes are used for pricing all publications. The code is determined by the number of pages in the publication. Information pertaining to the pricing codes can be found in the current issue of the following publications which are generally available in most libraries: *Energy Research Abstracts (ERA)*; *Government Reports Announcements* and Index (*GRA* and I); *Scientific and Technical Abstract Reports (STAR)*; and publication NTIS-PR-360 available from NTIS at the above address.

ACKNOWLEDGMENTS

The authors would like to gratefully acknowledge MEMC Electronic Materials, Inc. for providing epitaxial silicon materials, Showa Denko Silicon, K.K. for providing CZ silicon wafers, and SEMITEX Co., LTD. for providing a laser-microwave lifetime measurement system, LIFETECH-88®. A part of the work described in chapter 4 was contributed by Mr. K.Katayama, a visiting scientist at North Carolina State University.

TABLE OF CONTENTS

1 Introduction

Characterization of the chemical and electrical behavior of structural defects and impurities is a topic of great concern in optimizing semiconductor devices since they usually act as recombination centers, thereby reducing the minority carrier lifetime, a parameter central to device electrical performance. The inherent electrical activity of extended structural defects such as dislocations has been an issue addressed by researchers for many years [1-6]. The electrical behavior was initially discussed primarily in relation to the geometrical configuration of the defect, while the possibility of a defect decoration process was not strongly emphasized. Currently, there is still no clear answer as to whether, and to what degree, a clean structural defect will be electrically active. This is due to the fact that extended defects are very effective gettering sites for impurities introduced during crystal growth or during subsequent thermal treatment; hence they are always likely to be decorated to a certain extent. In this case an impurity-structural defect complex is responsible for the electrical activity, and its properties may be significantly different from those of a clean defect [7-9]. Currently at NCSU, the basic issues of minority carrier lifetime control and electrical activation and deactivation due to impurity gettering at defects is being studied by using a Si/Si(Ge) heterostructure which contains a controlled number of deliberately introduced misfit dislocations as a model system to simulate a variety of defect/impurity interactions which occur at more complicated and less spatially controlled interfaces. The recombination activity of "clean" and decorated dislocation related trap centers are revealed by a variety of techniques. Of these techniques, the contactless laser / microwave reflected power technique has been developed in a temperature dependent mode for recombination lifetime measurement and deep level spectroscopy.

In chapter 2, we describe the study of impurity gettering and electrical activity of misfit dislocations in epitaxial silicon grown with an addition of ~ 2% GeH_4 to a $SiCl_3H$ CVD reactor to provide a lattice misfit which is relieved via the formation of misfit

dislocations. The deleterious impurities such as Ni, Cu and Au were intentionally introduced from a backside deposited thin metal followed by rapid thermal annealing (RTA). Transmission Electron Microscopy (TEM) results indicate that the impurities were gettered along the misfit dislocations in near-surface regions either as Au precipitate colonies, or as $NiSi_2$ and CuSi silicide precipitates. Data from Scanning Electron Microscopy (SEM) in the Electron Beam Induced Current (EBIC) mode revealed that these precipitates dominate the recombination properties of the initially inactive misfit dislocations.

The impact of defects and impurities on minority carrier lifetime can be measured by numerous techniques such as the Electron / Light Beam Induced Current (EBIC/LBIC), light and dark Current -Voltage curves (I-V), Capacitance-Voltage-time (C-V-t), and diode Pulse Recovery (PR) as described in our last year annual report. However, in chapter 3 we describe a new development in the laser / microwave lifetime measurement system, LIFETECH-88®, which has advantages of contactless and non-destructive lifetime mapping over the entire wafer. This is especially important in solar grade materials since the wafer and final device are usually the same size. The system has two lasers which radiate at two different wavelengths allowing us to separate the surface and bulk components of recombination lifetime. The lifetime of epitaxial silicon wafers containing "clean", i.e. as-grown, and Ni or Au decorated misfit dislocations has been studied using the system.

The evaluation of the electronic defect levels associated with impurities by DLTS with respect to their carrier capture and emission characteristics is of utmost importance for understanding their electrical behavior. The qualitative information about energy levels can be obtained by measuring EBIC contrasts at various temperature since the EBIC contrast, i.e. recombination activity, directly corresponds with energy levels. In 4.1, we demonstrate the change in EBIC contrasts of metallic impurity decorated misfit dislocations at two

different testing temperatures. However one technique called laser / microwave deep level transient spectroscopy (LM-DLTS) has been developed to obtain the quantitative information about energy levels. This technique is based on an analysis of the temperature dependence of the photoconductance decay curve. The system is especially desirable for studying the energy level of as-grown defects since it requires no device fabrication. At the initial stage of this work, Laser/microwave deep level transient spectroscopy (LM-DLTS) was applied to characterize the energy levels of crystal defects in heat treated CZ silicon wafers with different [Oi], [Cs], and thermal history, which described in last chapter.

2 "Clean" and Decorated Dislocation

Si/Si-Ge heterostructures with misfit dislocations intentionally introduced in a controllable fashion have been studied for several years due to their potential for improving device performance. Recent reports indicate that dislocations may be applied not only as extrinsic gettering (XG) centers, but also as an active element of new semiconductor devices. The electrical, structural and chemical characterization of Si/Si(Ge) materials with misfit dislocations is thus an emerging issue for device fabrication. A study of gettering and electrical activity of metallic impurities Ni, Au and Cu has been carried out on epitaxial Si/Si(2%Ge)/Si wafers. The impurities were intentionally introduced from a backside deposited thin metal followed by rapid thermal annealing (RTA). Transmission Electron Microscopy (TEM) results indicate that the impurities were gettered along the misfit dislocations in near-surface regions either as Au precipitate colonies, or as $NiSi_2$ and CuSi silicide precipitates. Data from Scanning Electron Microscopy (SEM) in the Electron Beam Induced Current (EBIC) mode revealed that these precipitates dominate the recombination properties of the initially inactive misfit dislocation. The samples used in this study were n-type (100) Si wafers which contained a buried Si(Ge) heteroepitaxial layer between a pure Si capping layer and the substrate. The epitaxial layers of Si(Ge) and Si were grown at 1120°C in a chemical vapor deposition system (CVD) by adding approximately 2% GeH_4 to a $SiCl_3H$ CVD reactor. Two interfacial misfit dislocation (MD) planes were generated due to the lattice mismatch between Si and the buried Si(Ge) layers. The location of the MD interfaces varied from 3 to 5 mm beneath the top surface, while the MD density was controlled in the range of 10^6 to 10^8 cm^{-2}. The 60° misfit dislocations provided a heterogeneous nucleation site for impurity gettering. The impurities (Ni, Au, Cu) were introduced into the sample by thermally evaporating a thin metal layer film on the backside of the sample, followed by a rapid thermal anneal for 30 seconds at temperatures ranging from 800°C to 1150°C. RTA was carried out in an Ar ambient in an AG Heatpulse 210T

system equipped with high intensity tungsten-halogen lamps. SEM in the EBIC mode was performed on both as-grown and metal decorated samples to investigate the recombination activity of the impurity/dislocation complexes. The electron beam energy was varied from 10 to 25 KeV to obtain electrical information at different depths. A gold film of about 200Å thickness was thermally evaporated on top of the sample through a shadow mask to form the Schottky contact for the EBIC/SEM measurement. Finally, both plan view and cross-section TEM were performed to reveal the microscopic details of the impurity/defect structures.

2.1 Electrical Activity

An EBIC examination of the as grown Si on Si(Ge) on Si structure used in this work, see Fig. 1a, did not reveal any misfit dislocation contrast at all. However, surface traces of the misfit dislocations were visible on the top surface of the same sample using a Nomarski optical microscope, as shown in Fig. 1b, which indicates that the electrical activity of as-grown misfit dislocations is very low, certainly below the EBIC detection limits at room temperature. The dislocations were then decorated with Ni, Au and Cu by diffusion from a back side evaporated layer via rapid thermal annealing for 30 seconds. The temperature range from 400°C to 1200°C was examined in order to achieve different levels of defect decoration. Significant differences in electrical activity of decorated dislocations have been observed as a function of the metal and the temperature of annealing. An EBIC image obtained for a Ni sample contaminated at 1000°C is shown in Fig.2a and reveals that: 1) EBIC contrast occurs as dark spots for all annealing temperatures; 2) dislocation lines are not visible between the spots; 3) the density of dark spots increases with the increase of annealing temperature. The dark EBIC contrast of the Ni contaminated samples indicates that localized recombination centers are now present along the misfit dislocations.

The gold decorated dislocations gave a detectable continous EBIC contrast after annealing at or above 800°C, whereas no contrast was evident at 600°C. An example of

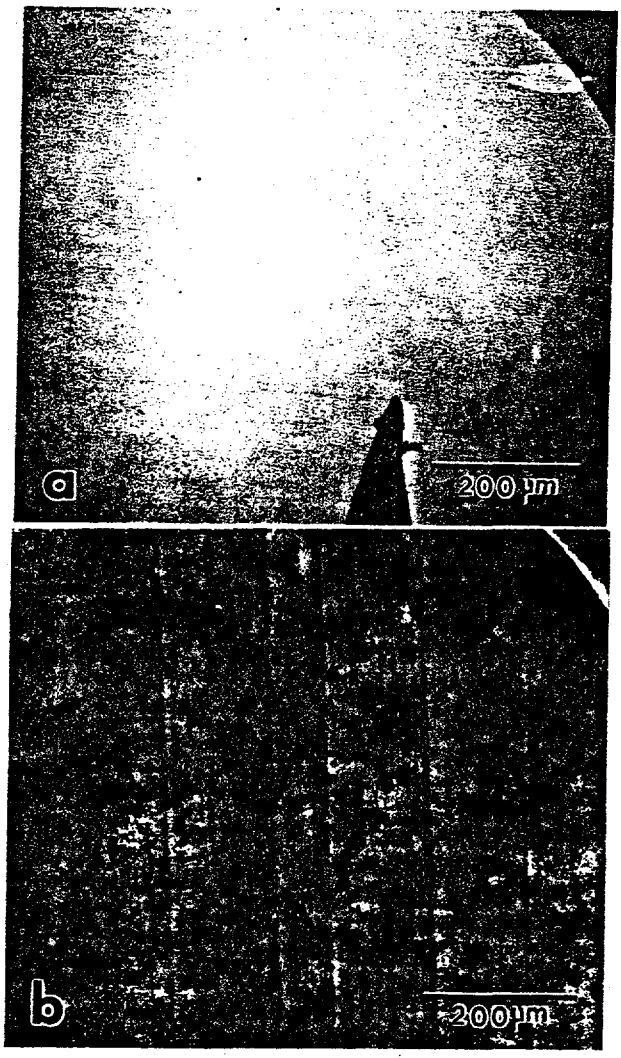

Fig. 1 **a** EBIC/SEM image of an as-grown heteroepitaxial structure showing no contrast from buried interfacial misfit dislocations, **b** Nomarski optical micrograph of the same area.

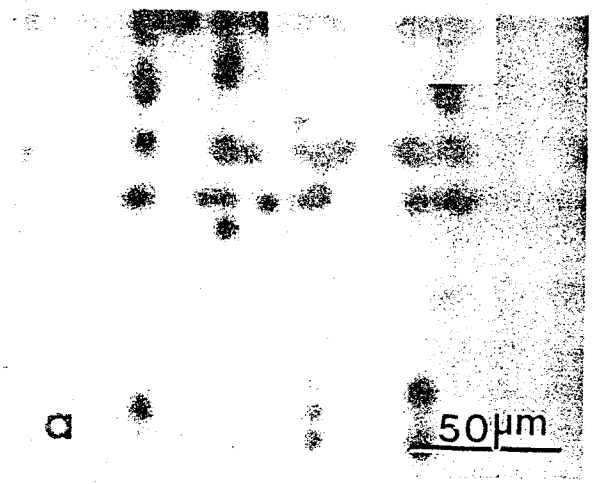

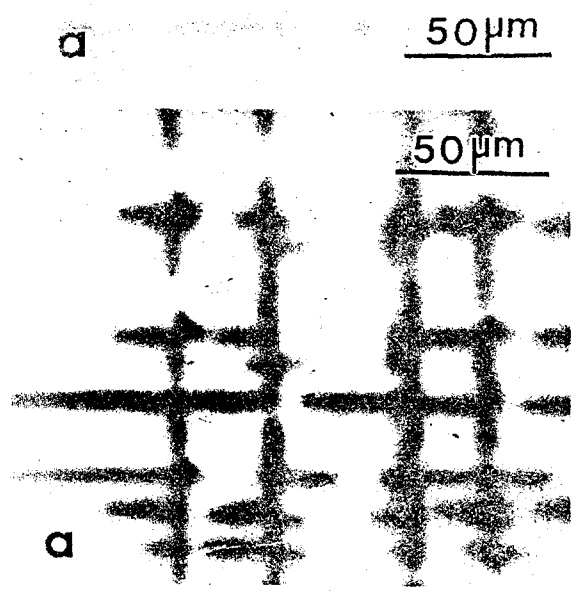

Fig.2 SEM/EBIC image of **a** Ni, **b** Au and **c** Cu decorated misfit dislocations (RTA at 1000°C for 30 seconds)**b**. Bright field cross-section TEM of the same sample showing Au precipitate colony at a MD interface

dislocations decorated at 1000°C is given in Fig.2b At higher diffusion temperatures the dislocations appear as continous dark lines indicating that they are active recombination centers along their total length.

Finally, the electrical activity of Cu decorated misfit dislocations was also examined with EBIC, as shown in Fig.2c, for a sample annealed at 1000°C. The Cu decorated misfit dislocations become electrically active with a characteristic dark crossed shape which indicates that these recombination centers form more readily at the intersections of two dislocations, and then extend out along the individual dislocation lines

2.2 Structural Analysis

Performing TEM studies, we found that these recombination centers resulted from the formation of Ni precipitates along the MD, or in the immediate vicinity of the dislocation. Figure 3a is a cross-section bright field TEM micrograph for the Ni contaminated sample annealed at 1000°C, showing an octahedral precipitate which presumably nucleated at the MD interface. The precipitate size was approximately 500nm and the precipitates were separated by a distance of several tens of microns. From energy dispersive x-ray spectroscopy and electron diffraction pattern analyses, these precipitates were identified as the epitaxial disilicide ($NiSi_2$) with cubic CuF_2 structure. Furthermore, it was observed from the micrograph that a large number of dislocations were generated around the precipitates. These secondary dislocations might result from: 1) the 0.4% lattice parameter mismatch between $NiSi_2$ and Si; 2) the internal hydrostatic stress caused by volumetric contraction of $NiSi_2$ precipitate; 3) the difference in thermal expansion coefficient of the silicide and silicon during the fast RTA cooling.

These misfit dislocations were decorated uniformly with Au as shown by the TEM data in Fig.3b, which is a cross-section bright field TEM image of a MD interface of the same Au diffused sample. The Au precipitate colonies found along the misfit dislocation are very similar to those formed during conventional furnace annealing, as reported

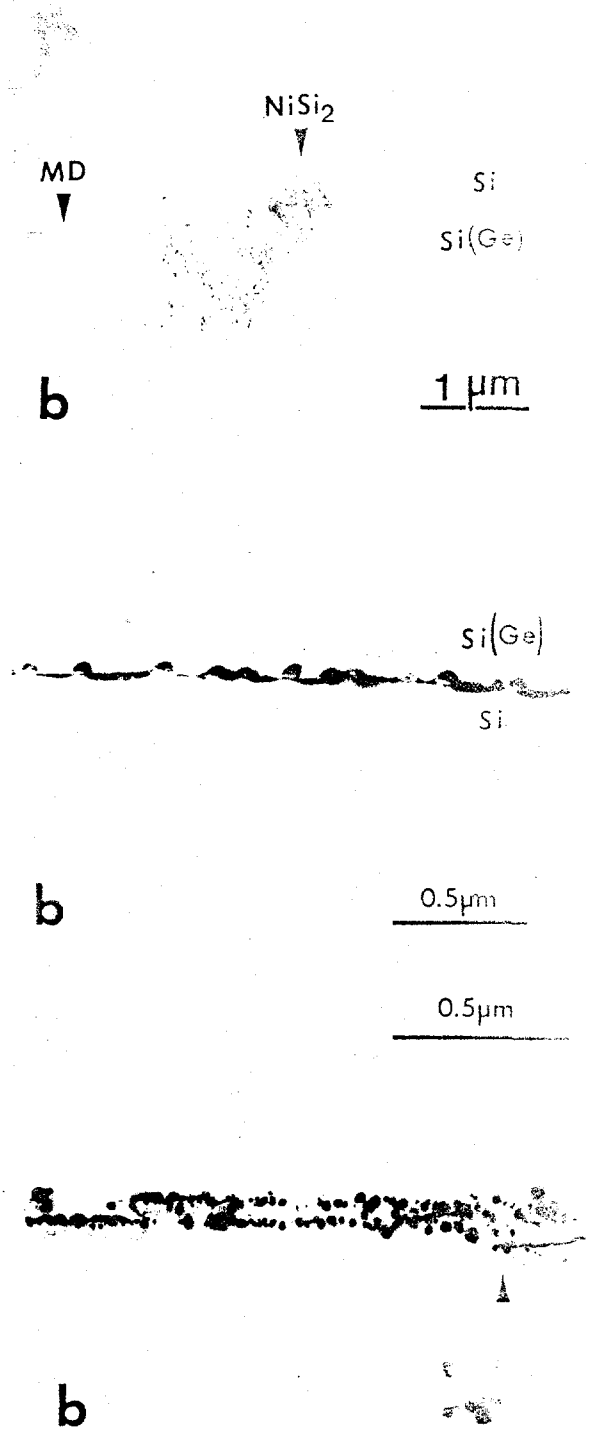

Fig.3 Bright field cross-section TEM showing **a** $NiSi_2$ precipitate and **b** Au precipitate colony at a MD interface, and **c** Bright field Plan-view TEM showing CuSi precipitates.

previously[10]. Since the precipitate size was ~ 50 nm with a separation of 100nm to 200nm, as we know, the much lower resolution of EBIC in Fig.2b (~ 5μm in this particular case) shows the Au precipitate colonies as continuous lines.

A plan-view TEM study, see Fig.3c, showed that spherical precipitates formed along the misfit dislocation. The precipitates were found to have a typical Moiré fringe contrast, as shown in the superimposed micrograph in Fig.3c, indicating that they were crystalline. These precipitates were very similar to those formed under similar experimental conditions and previously identified as cubic CuSi silicide precipitates [11].

2.3 Discussion

It is well recognized that the MD strain field results in a reduction in the nucleation barrier for localization of a diffusing impurity, and then the misfit dislocations act as effective heterogeneous nucleation sites. In our study, the impurities were found to be gettered by MD during RTA in the form of $NiSi_2$, CuSi and Au precipitates. We should notice that the $NiSi_2$ and CuSi precipitates have crystal structures similar to the Si substrate and that the precipitation processes consume Si atoms. Both factors can lead to an internal epitaxial growth with enhanced precipitate nucleation and growth. Comparing Fig.3a and Fig.3c, it is obvious that the $NiSi_2$ density was orders of magnitude lower that that of CuSi, but the precipitate size was much larger. This result indicates that Ni precipitates were difficult to nucleate but once nucleated grow very fast, while Cu precipitates are easily nucleated but are difficult to grow. As we know, the precipitate nucleation is controlled by the driving force, i.e. the free energy, while the growth of the new phase can be affected by the diffusion of the impurity. However, in order to explain the difference between Ni and Cu, more quantitative studies need to be performed. Very different from Ni or Cu, Au does not form silicide with silicon; therefore a lower precipitation growth rate is expected. This is because the precipitates have to eject Si atoms into interstitial sites thus resulting in a

large strain associated with the precipitation. This can explain the TEM result of Fig.3b, which shows the presence of small Au precipitates.

Comparing the electrical activities of decorated and "clean" misfit dislocations, the as-grown misfit dislocations show no EBIC recombination activity due to their intrinsic structure. One possible explanation is that if the energy level of misfit dislocation is relatively shallower, the recombination activity will not be as efficient as that of the energy level present at the middle of the band gap. Our EBIC study on contaminated samples indicates that the misfit dislocations are electrically activated by gettered impurities and the precipitation is responsible for the strong recombination activity. The EBIC images of decorated MD's with different impurities depend on the distribution of the precipitate at MD interfaces. Therefore, the mechanism of recombination activity related to these precipitates must take into account the following factors: 1) existence of a space-charge region (electrical field) around the precipitates which could increase the effective capture cross section of minority carriers, thus increasing the local recombination rate; 2) deep levels due to the precipitation related defects such as point defects or their aggregates, and secondary dislocation generation as occurs with $NiSi_2$. The most likely mechanism is probably a combination of both factors. The space-charge region increases the captured flux of carriers, and the precipitation related defects introduce deep levels. These are two important parameters affecting the recombination rate and ultimately the EBIC contrast.

3 Impact of Defects and Impurities on Minority Carrier Lifetime

3.1 Bulk and Surface Components of Recombination Lifetime

Recently, contactless, high throughput, nondestructive techniques have been of particularly interest.[12,13] The microwave absorption/reflection (MR), [14,15] infrared absorption (IA) [16,17], photoconductance (PC) [18] or pseudo-contactless open-circuit voltage decay (OCVD) [19] methods are commonly used for noncontact recombination lifetime study. In all these techniques laser illumination is used to generate excess electron-hole pairs. A signal decay, which carries information about recombination properties of material, is then monitored after the laser radiation is turned off. This signal is proportional to the number of carriers integrated over the entire volume of probed material (in the MR, PC or IA) or to the gradient of carriers at a depletion layer edge (for the OCVD technique). The decay signal can be described by complicated mathematical formulae generally in the form of an infinite series of exponentially decaying time-dependent terms, each characterized by its own constants. [12,13,16,20] From these constants, both the surface as well as the bulk contributions can be extracted. However, the extraction procedure is not straightforward, especially for modern materials with extremely high bulk lifetimes of the order of 1 ms, and there is no one single reliable method to separate the surface and bulk components of recombination lifetime. [20,21] In this work an algorithm has been developed for recombination lifetime analysis based on two measurements of the sample excited consecutively by two lasers with different wavelengths. The algorithm was tested experimentally in conjunction with a microwave absorption/reflection technique on bare and oxidized CZ silicon material. The surface and bulk recombination components were obtained by applying the algorithm to the experimental data. The algorithm developed here for the separation of surface and bulk components of recombination lifetime takes advantage of the fact that the surface and bulk contributions vary if the shape of the

generation function changes. This change is introduced by using two excitation lasers with two different wavelengths. Since the absorption coefficient is a strong function of wavelength, see Eq. (2), the electron-hole pair generation varies with wavelength and the initial bulk carrier density profiles are affected by surface recombination differently. For the theoretical analysis of the separation problem the basic relationship describing the average (volume integrated) density of excess minority carriers vs. time is taken after Ref. 20. This equation is a solution, under low excitation conditions, of the time dependent carrier transport problem for the case of a wave light is used to generate electron-hole pairs. The surface recombination velocity S is assumed to be the same at both sides of a wafer of thickness d. The original formulae, see Eq. (7b) in Ref. 20, are rewritten here to allow the boundary condition that the function maximum occurs at time τ=0, and also to show the explicit influence of laser wavelength:

$$N(\lambda,t) = \frac{8\, G_0 \exp\left(\frac{-\alpha_\lambda d}{2}\right)}{d\, T} \sum_{n=1}^{\infty} B_n(\lambda) \exp\left(-\frac{t}{\tau_n}\right) \qquad (1a)$$

$$N_{rel}(\lambda,t) = \frac{N(\lambda,t)}{N(\lambda,0)} \qquad (1b)$$

$$B_n(\lambda) = \frac{\sin\frac{\alpha_n d}{2}\left[1-\exp\left(-\frac{T}{\tau_n}\right)\right]}{\frac{1}{\tau_n}\left(\alpha_\lambda^2+\alpha_\lambda^2\right)\left[\alpha_n d+\sin\left(\alpha_n d\right)\right]} \times$$

$$\times \left[\alpha_\lambda \sinh\left(\frac{\alpha_\lambda d}{2}\right)\cos\left(\frac{\alpha_n d}{2}\right)+\alpha_n \cosh\left(\frac{\alpha_\lambda d}{2}\right)\sin\left(\frac{\alpha_n d}{2}\right)\right] \qquad (1c)$$

$$\frac{1}{\tau_n} = \frac{1}{\tau_b} + \frac{1}{\tau_{ns}} \tag{1d}$$

$$\frac{1}{\tau_{ns}} = \alpha_n^2 D \tag{1e}$$

where:

$N(\lambda,t)$	-	average density of excess minority carriers
d	-	wafer thickness
T	-	pulse duration time
α_l	-	absorption coefficient
D	-	diffusion coefficient
α_n	-	roots of F(a) function
τ_b	-	bulk lifetime
τ_n	-	n-th decay constant
τ_{ns}	-	surface component of n-th decay constant
S	-	surface recombination velocity
λ	-	laser wavelength
G_0	-	generation function

In this paper values of D = 30 cm^2/s, d = 525 μm, and T = 150 ns were used for calculations, unless otherwise specified. The absorption coefficient is related to the laser radiation wavelength by Eq. (2) (see Ref. 22)

$$\alpha_\lambda = \left(\frac{84.732}{\lambda} - 76.417\right)^2 \tag{2}$$

with the wavelength λ in μm and the absorption coefficient α_l in cm^{-1}.

The F(a) function is defined as follow:

$$F(\alpha) = \frac{\alpha D}{S} - \cot\frac{\alpha d}{2} \tag{3}$$

Example decay profiles of the normalized minority carrier density for the 1000 μs bulk lifetime value are presented in Fig. 4a using S as a parameter for family of curves. It can be seen that the decay shape is not only a function of bulk lifetime, but also depends strongly on the surface recombination velocity. In addition, the slope is not constant and for large values of S is much higher in the initial part of the decay. This slope, called an instantaneous observed lifetime τ_0 [20] has two terms; the first one is the time independent bulk lifetime τ_b, and the second represents a time-dependent surface component R_S

$$\frac{1}{\tau_0} = \frac{1}{\tau_b} + R_s(\lambda, S) \tag{4}$$

where

$$R_s = -\frac{d}{dt} \ln \left[\sum_{n=1}^{\infty} B_n \exp\left(-\frac{t}{\tau_{ns}}\right) \right] = \frac{\sum_{n=1}^{\infty} B_n \frac{1}{\tau_{ns}} \exp\left(-\frac{t}{\tau_{ns}}\right)}{\sum_{n=1}^{\infty} B_n \exp\left(-\frac{t}{\tau_{ns}}\right)} \tag{5}$$

Plotting the data of Figs. 4a and in terms of the normalized instantaneous lifetime τ_0/τ_b yields the families of curves in Fig. 4b. It can be seen in Fig.1b that the instantaneous lifetime asymptotically reaches its maximum value for time $\tau \to \infty$. However, since τ_b is not a function of time, the asymptotic instantaneous lifetime can be denied from the asymptotic value of R_{sa} (limit of R_S for $\tau \to \infty$) equal to

$$R_{sa} = \frac{1}{\tau_{1s}} \tag{6}$$

This is because the series $\tau_{1s}, \tau_{2s}, ..., \tau_{ns}, ...$ is decreasing. Finally, the bulk lifetime τ_b is then given by Eq. (7)

$$\tau_b = \frac{\tau_{0a}\tau_{1s}}{\tau_{1s} - \tau_{0a}} \tag{7}$$

where τ_{0a} is the limit of τ_0 for $\tau \to \infty$.

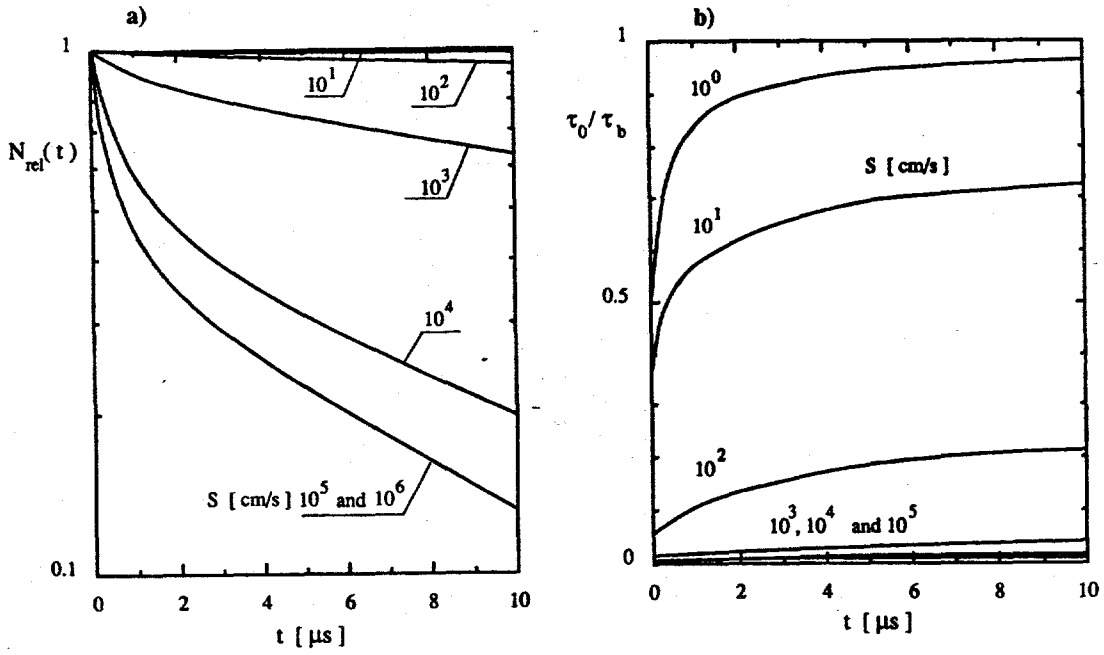

Fig.4 Decay profiles of **a** normalized minority carrier density N_{rel} (t) for different values of S, with λ=0.91 μm and τ_b = 1000 μs, and **b** the corresponding relationship of normalized instantaneous lifetime

It is evident from Eq. (7) that in order to obtain the bulk lifetime τ_b, the surface component τ_{1s} must be found. There are two relatively simple cases when the surface component can be easily calculated, without the S value need be known. First, the very low recombination velocity case (S→0), when $\tau_{1s} \rightarrow \infty$ and $\tau_b = \tau_{0a}$. Second, for the very high S ($S \rightarrow \infty$), where τ_{1s} is equal to $\pi^2 D / d^2$. For the middle range of S, τ_{1s} depends on S, and the S value is a prerequisited for further calculations. This value can be obtained by analysis of the influence of laser wavelength on decay curves, an example of which is shown in Fig.5, where the decay profiles of normalized minority carrier density for several laser wavelengths are presented, with S and τ_b equal to 10^5 cm/s and 10 μs, respectively. It can be seen that there is a separation d, between the individual decay curves for each pair of laser wavelengths. The value of d in Fig. 5 increases with time and approaches its asymptotic value d_a. It is important to notice that the asymptotic d_a is only a function of surface recombination velocity and not of the bulk lifetime. Therefore, this function can be used to estimate the surface component of lifetime, if we define the d function as in Eq. (8)

$$\delta = \ln \left[\frac{N_{rel}(\lambda_1, t)}{N_{rel}(\lambda_2, t)} \right] \tag{8}$$

and since

$$\ln N(\lambda, t) = -\frac{t}{\tau_b} + \ln \left[A \sum_{n=1}^{\infty} B_n(\lambda) \exp\left(-\frac{t}{\tau_{ns}}\right) \right] \tag{9}$$

we have

$$\delta = \ln \frac{\sum_{n=1}^{\infty} B_n(\lambda_1) \exp\left(-\frac{t}{\tau_{ns}}\right)}{\sum_{n=1}^{\infty} B_n(\lambda_2) \exp\left(-\frac{t}{\tau_{ns}}\right)} \quad \frac{\sum_{n=1}^{\infty} B_n(\lambda_2)}{\sum_{n=1}^{\infty} B_n(\lambda_1)} \tag{10}$$

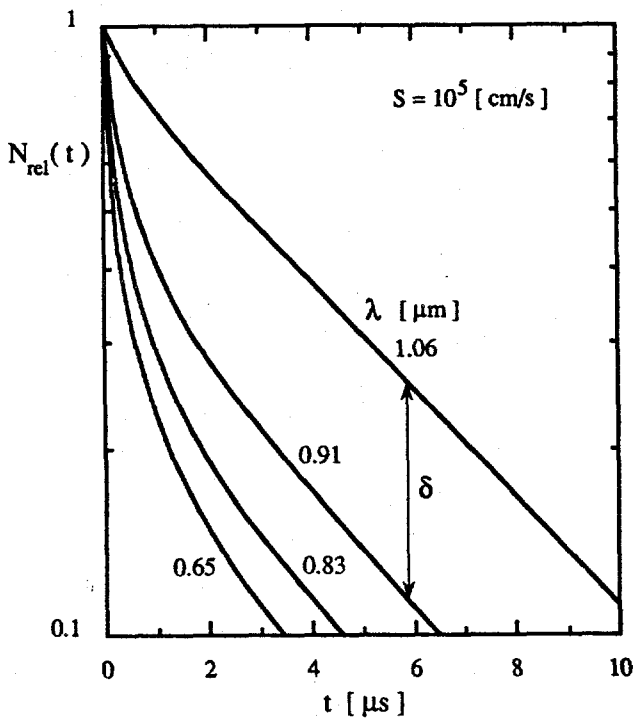

Fig.5 Decay profiles of the normalized minority carrier density for different values of wavelength λ and wafer thickness d = 525 μm. The decay separation is denoted by δ.

and for the same reason as in Eq. (6), the limit of d is constant and equal to

$$\delta_a = \ln \frac{B_1(\lambda_1)}{B_1(\lambda_2)} \quad \frac{\sum_{n=1}^{\infty} B_n(\lambda_2)}{\sum_{n=1}^{\infty} B_n(\lambda_1)} \tag{11}$$

The separation function d is plotted vs. time for different values of S in Fig. 6. The function reaches 95% of its asymptotic value after approximately $\tau = 5$ μs for a variety of surface recombination velocities. The d_a dependence on surface recombination velocity S is presented in Fig. 7 for selected combinations of laser wavelengths. It is clear that a wide range of S can be evaluated from d_a. As expected, the separation increases if the difference between two laser wavelengths increases. The upper level of detected S is approximately 10^5 cm/s, since the investigated function saturates at this value. The lower limit of detectable S depends on resolving each of the two decays (noise problem), and can be estimated as 100 cm/s assuming a 100:1 signal to noise ratio. Figure 4 is a key issue of the proposed technique since it ties the decay separation d, to the surface recombination velocity S. The relation presented in Fig. 7 is a simple function of the specific components of equipment (installed laser wavelengths) and the wafer thickness d. The influence of d on d_a is relatively weak within the range of useful wafer thicknesses, i.e. 300 μm to 1mm. For a given value of S, the bulk lifetime and asymptotic value of instantaneous lifetime are related through Eq. (7), as shown in Fig. 8. Note that small changes in τ_{0a} may make a big difference in bulk lifetime value, particularly for high surface recombination velocity. Therefore, very accurate measurements of τ_{0a} and S are required. Finally, some comments about correct interpretation of the experimentally measured decay with regard to trapping effects must be made in so far as recombination vs. emission is concerned. This effect is of particular interest at the later part of decay and is also accounted for in the proposed algorithm. It is possible that a change in the slope of the decay curve may result from

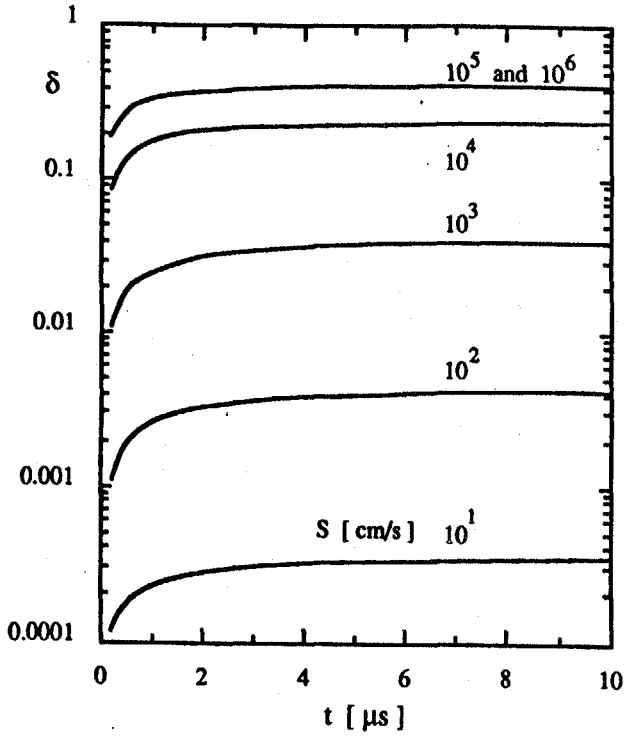

Fig.6 Decay separation function vs. time for different values of S, and combination of laser wavelengths λ_1 = 0.91 μm and λ_2 = 0.83 μm

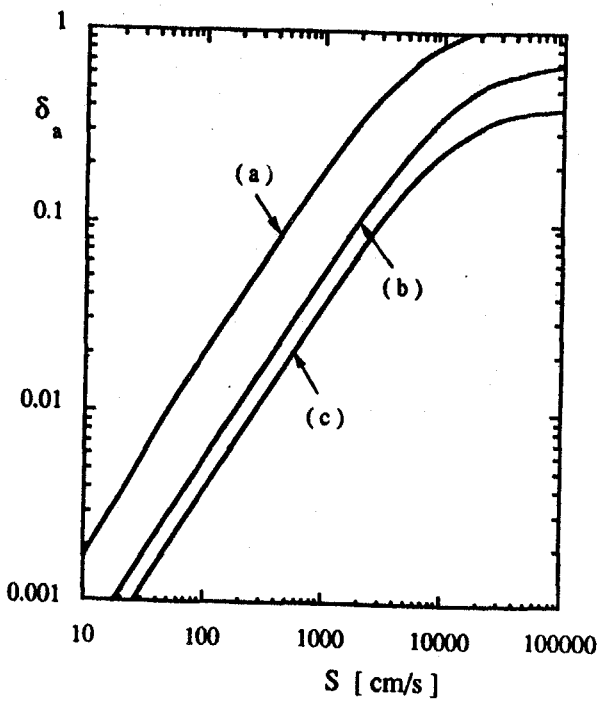

Fig.7 Asymptotic value of decay separation as a function of surface recombination velocity with parameter being a combination of laser wavelengths, (a) λ_1 = 1.06 μm and λ_2 = 0.65 μm (b) λ_1 = 1.09 μm and λ_2 = 0.91 μm and (c) λ_1 = 0.91 μm and λ_2 = 0.83 μm for d = 525 μm

varying contributions of capture and emission processes at the mid- and later parts of decay, respectively. The possible interference of trapping effect, which will degrade the measurement accuracy, can actually be determined by checking the influence of temperature increase on the instantaneous lifetime value. This occurs because at elevated temperature, the recombination process is slowed down while the emission is enhanced; however, this solution is not always straightforward, especially within the transition range between the two phenomenons. For such a case the experimental separation function reaches its maximum and then decreases at the later part of the decay.

The algorithm for separating the minority carrier lifetime into bulk and surface components requires experimental measurements of the $d_{a\ exp}$ and $t_{0a\ exp}$. The surface recombination velocity is then obtained from $d_{a\ exp}$ through Fig.7, or via Eq. 11. Once S is known, the surface component of lifetime can be calculated using Eq. (3) to obtain α_1, and Eq. (1e) to determine the surface component τ_{1s} itself. Finally, the bulk lifetime is calculated from Eq. (7) or Fig. 8. The above algorithm was experimentally verified using the microwave reflectance LIFETECH-88® system. [13,23] The system contains two lasers operating at the wavelengths, $\lambda_1 = 0.91$ μm and $\lambda_2 = 0.83$ μm, respectively with the laser pulse width equal to 150 ns. The time constant of the microwave system itself, including amplifier, is of the order of 100 ns. The signal to noise ratio, which results mainly from the amplifier noise and low level of electron-hole pair generation, is typically better than 100:1. The vertical signal resolution is limited by the 8 bit A/D converter (256 levels) of the 2430A Tektronix® oscilloscope, used with the system.

A commercially available, n-type, (100) orientation, 20 Ωcm resistivity, 650 μm thick, CZ-silicon wafer was used for the experiment. The silicon wafer was initially annealed in N_2 +5% O_2 ambient in order to growth a 600 μm thick oxide and the decay signal was measured on the oxidized wafer. Then, the oxide was removed with buffered HF solution, and measurements were repeated consecutively over a 30 minutes period, as well as 24 hours after the etching process. In this way three different surface conditions

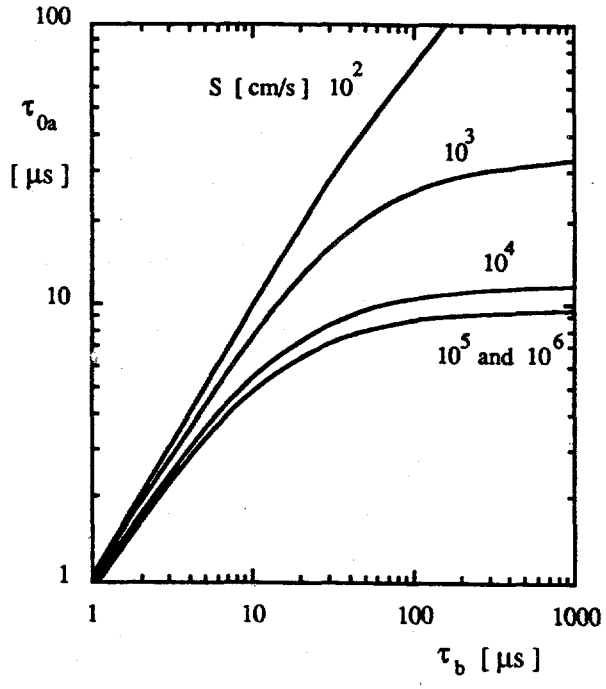

Fig.8 Bulk lifetime as a function of asymptotic value of instantaneous lifetime for different values of surface recombination velocity S

were obtained on a wafer with the same bulk lifetime value. Experimental data and theoretical fitting for three pairs of normalized carrier decays (3 surface conditions x 2 laser wavelengths) are presented in Fig.9 and the results are summarized in Table 1. A fairly

Table 1. Comparison of experimental and theoretical results

	Process	$t_{oa}(l_1)$ [μs]	$t_{oa}(l_2)$ [μs]	d_a	S [cm/s]
experiment	with oxide	43.2	44.6	below detection	<100
	30 mins after etching	18.4	18.15	0.1	1800
	24 hrs after etching	12.8	12.2	0.4	12000
theory	with oxide	44.5	44.5	<0.001	1
	30 mins after etching	17.45	17.45	0.11	2000
	24 hrs after etching	12.61	12.61	0.35	8000

good agreement between theoretical and experimental data was obtained; however slightly higher than expected separation values are observed in the experiment, especially for the case of high surface recombination velocity. This tendency is characteristic for all measurements made with this equipment. We believe that it results primarily from a deviation of the specified peak intensity wavelengths in the laser diodes used (LA-160 and LD-160 series, M/A-Com Laser Diode, Inc.), and/or discrepancies between the actual and theoretical absorption coefficients given by Eq. (2).

3.2 Lifetime Analysis for "Clean" and Decorated Si/Si(Ge)

To study the impact of "clean" and decorated dislocation on minority carrier lifetime, we have applied the laser/microwave reflectance (LM) [24-26] technique as a noncontact tool for electrical, and full wafer X-ray topography (XRT) imaging for structural analysis. The recombination lifetime over a temperature range from 20°C to

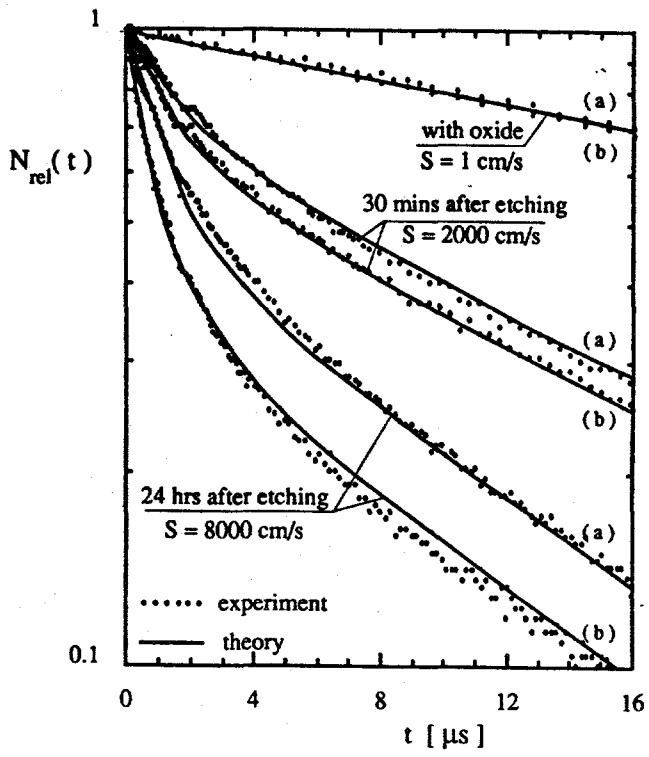

Fig.9 A comparison of experimental data and theoretical decay profiles for a CZ crystal with three different surface conditions and laser wavelengths equal to a) $\lambda_1 = 0.91$ μm and b) $\lambda_2 = 0.83$ μm

220°C in 5°C steps, and the dislocation distribution were analyzed with these techniques, respectively. Also, the deep energy levels associated with dislocations were obtained from the temperature dependence of the recombination lifetime [27]. A correlation between the electrical activity of misfit dislocations and their density was found. Electrical activities of misfit dislocation in as-grown material and material subjected to ion- implantation with metals followed by rapid thermal annealing (RTA) were compared. A gettering effect of the dislocations was observed in this electrical properties.

The samples were fabricated by epitaxial CVD growth of 2 μm thick SiGe(1%) layer on n-type, Sb-doped, 10-15 Ωcm, <100> oriented, 4 inch diameter silicon substrate. The Si(Ge) layer was capped by subsequent epitaxial growth of a 3 μm thick silicon layer. In this way, two misfit dislocation (MD) networks at the Si-Si(Ge) plane boundaries were introduced in a controllable fashion, as shown in Fig.10. The dislocation density varied with the amount of Ge incorporated into the epitaxial layer, and the network location with the thickness of epitaxial capping layer. In order to observe the gettering properties of MD and changes in electrical activity after decoration, a set of three wafers was prepared. This included two wafers implanted from the back side with gold or nickel, with dose C_S = $10^{12}/cm^2$ at an energy E = 100 keV. The reference wafer was not implanted. As results from our previous study [28-30] indicated, these two metals have significantly different mechanism of gettering at MD, and they were expected to influence the dislocation "core" and its electrical activity in different ways. Following the implantation process, a cross-grid network of MD over the entire wafer was observed nondestructively with large-area XRT topography. A map of the corresponding recombination lifetime was also measured. Then, the wafers were cut into four quarters. Three quarters were annealed with RTA at temperature 400°C, 800°C and 1000°C for 30 seconds, respectively. A fourth reference quarter was not annealed. The location of quarters with respect to annealing temperature is presented in Fig. 11. The commercially available LIFETECH-88® (SEMITEX Co., Ltd.)

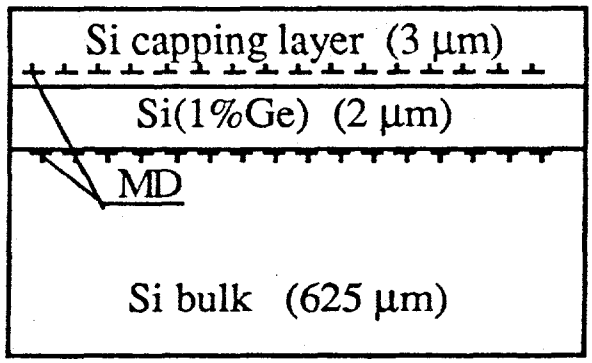

Fig.10 Schematic diagram of Si/Si(Ge)/Si heterostructure with MD planes.

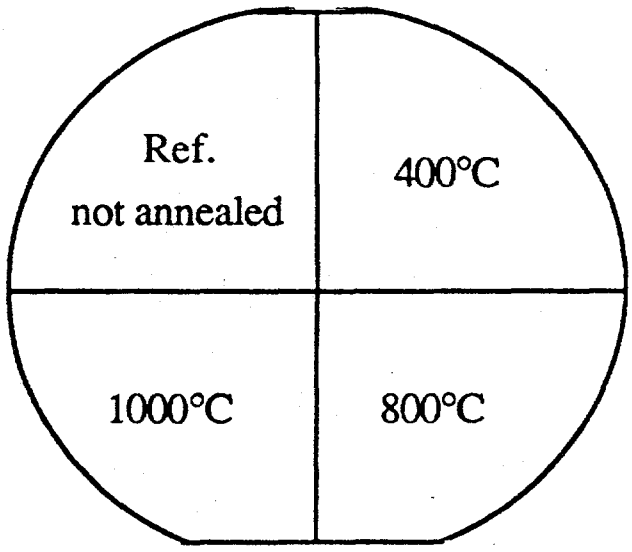

Fig.11 Annealing conditions for studied Si/Si(Ge)/Si heterostructures (annealing time t=30 seconds).

and the GX 21 (Marconi Avionics) systems were used for recombination lifetime and X-ray topography measurements, respectively.

Figure 12 shows the cross-grid network of misfit dislocations obtained with XRT for the reference (not implanted) wafer. Note the presence of both localized bands with high dislocation density, as well as relatively more uniform and dense MD networks. The similar pattern of MD was also observed for wafers implanted with metals, although the location of MD bands is unique for each wafer and believed to be related to the condition of the wafer edge. The corresponding map of initial "effective" lifetime (e.g. before RTA process), defined here as a slope of the later part of the decay signal is shown in Fig.13. The average value of lifetime measured at room temperature was 20 μs and a cross pattern with a depressed lifetime value of 9 μs was detected, which can be matched to the local variation of dislocation density, see regions marked with an A carrier transport and LM reflectance theory [31,32], that this "effective" lifetime includes both a bulk and surface component, resulting from the volume distribution of defects and their effect on recombination processes. We assumed that the two dimensional MD dislocation network, characteristic of a studied Si/Si(Ge)/Si heterostructure, is responsible for an enhanced surface recombination velocity which dominates the surface component of lifetime. This is because the penetration depth of the laser beam (λ=830 nm) used in this study is significantly deeper than the epi/substrate MD networks (3 μm and 5 μm), and additionally the Si(Ge) epilayer has negligible thickness in comparison to the bulk wafer. Taking into account the above experimental conditions, we interpret the minority carrier recombination due to the MD layers as "surface", and that due to the bulk defects as "bulk" recombination. These two lifetimes were separated and studied independently using the procedure proposed in Ref. 31 which takes advantage of the laser wavelength l influence on carrier decay N(t), as schematically presented in Fig. 14.

Insofar as the bulk and surface lifetime measured at room temperature are concerned, the initial recombination properties of reference, gold and nickel implanted

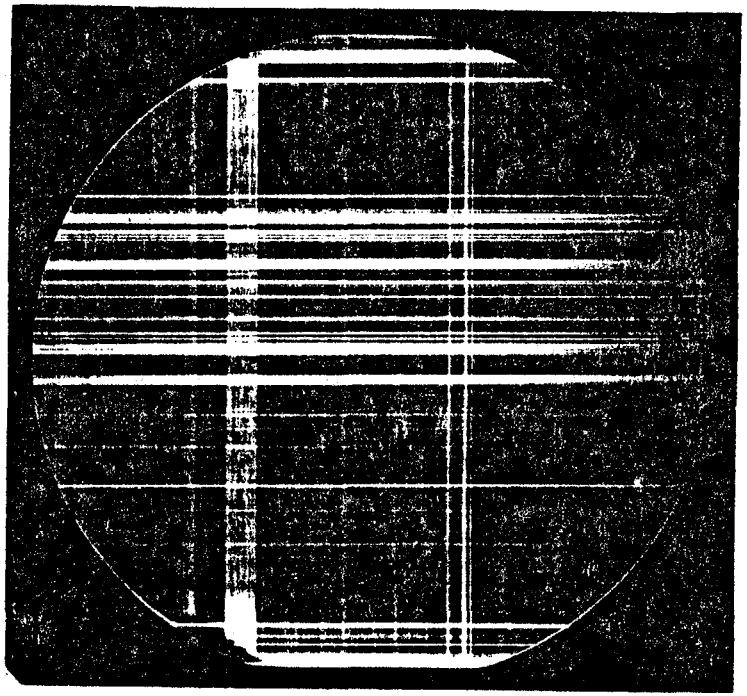

Fig.12 Transmission X-ray topograph of the XG Si/Si(Ge)/Si heterostructure.

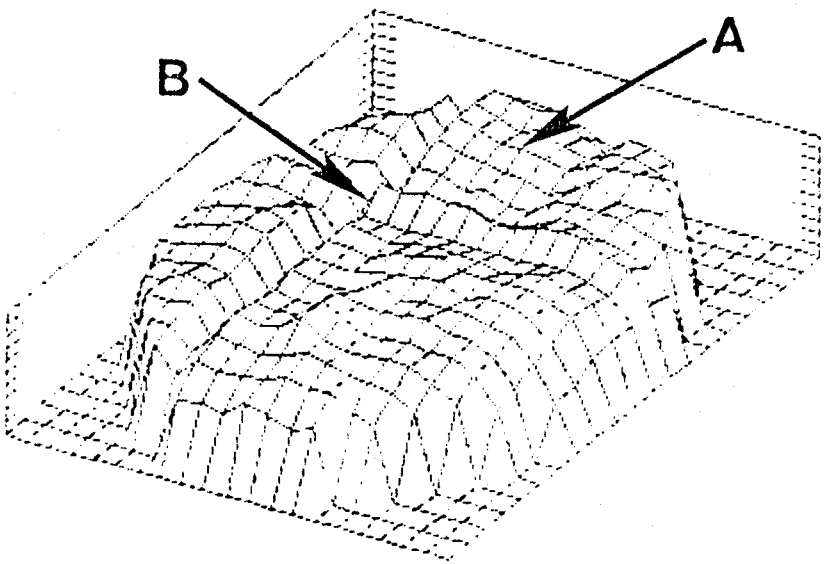

Fig.13 Map of initial recombination lifetime measured at room temperature for the XG reference wafer shown in Fig.12

samples were similar. However, the temperature dependence of lifetime was unique for each contaminant introduced. The results are presented in Fig. 15, where the temperature scan of lifetime components is shown. The differences in the temperature scan slope, interpreted as activation energy and marked with solid lines, reflect the differences in traps location within the forbidden gap, as discussed in Ref. 27. In Fig. 15, superscripts at the sample identification mark denote the activation energies of the recombination process, while subscripts refer them to the appropriate lifetime component. After RTA, the sample quarters were reassembled and the recombination lifetime measurements were repeated. A map of lifetime similar to the one of Fig. 13 showing the reference XG wafer (not metal implanted) is presented in Fig. 16. Unexpectedly, the quarter annealed at the highest temperature revealed the highest value of lifetime measured at room temperature, see Fig. 16 a. We have attributed this effect not only to MD or a metal/ MD complex, but mainly to RTA process which introduces a number of defect complexes which are responsible for capture and re-emission of recombining carriers generated by light. Such a recombination process is recognized as a trapping effect [33]. In the specific case described here, we believe that the trapping sources are not only related to vacancies/ interstitials/ contaminants present within the wafer, but in addition to a depletion layer formed around the MD, or at the surface. This layer is filled with carriers during the laser pulse and then emptied during signal decay. As a result, an increase in lifetime within the material can be observed. This lifetime is controlled by generation (emission) rather than recombination (capture) process. The trapping effect may be reduced at elevated temperatures; compare Figs. 16 a and b.

Notice that the electrical activity of near surface MD and in the bulk were strongly affected by RTA even if there was no metal implanted. The presence of Au and Ni contaminants additionally modify the MD recombination properties, see Fig. 17a and b, where the influence of annealing temperature (metal decoration level) on the bulk and surface component of lifetime is shown, respectively. In order to avoid the trapping effects,

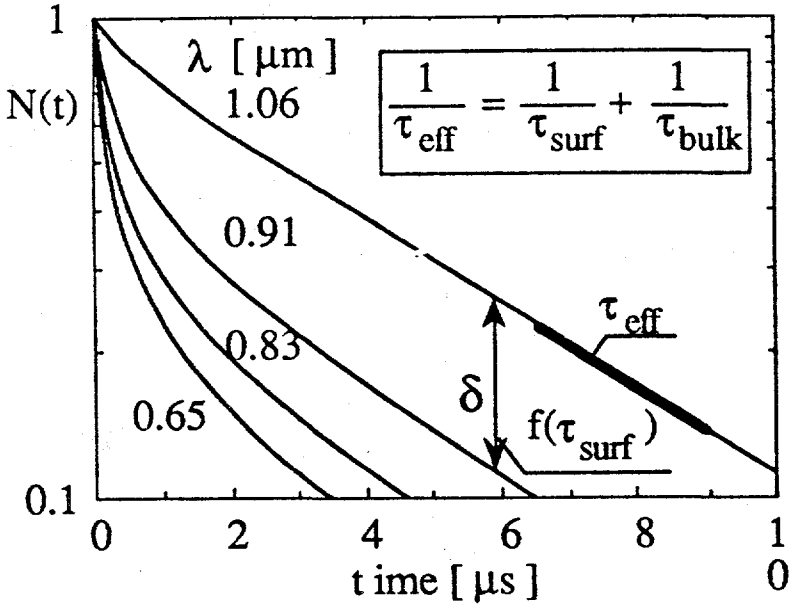

Fig.14 Minority carrier decays with laser wavelength as a parameter.

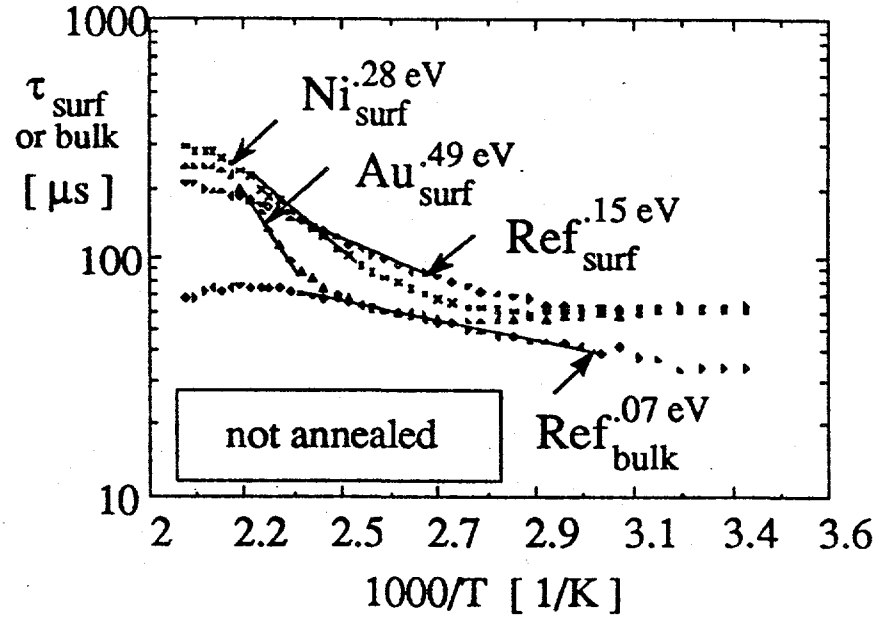

Fig.15 Dependence of the bulk and surface recombination lifetime vs. measurement temperature for the XG Si/Si(Ge) sample implanted with metal before RTA process.

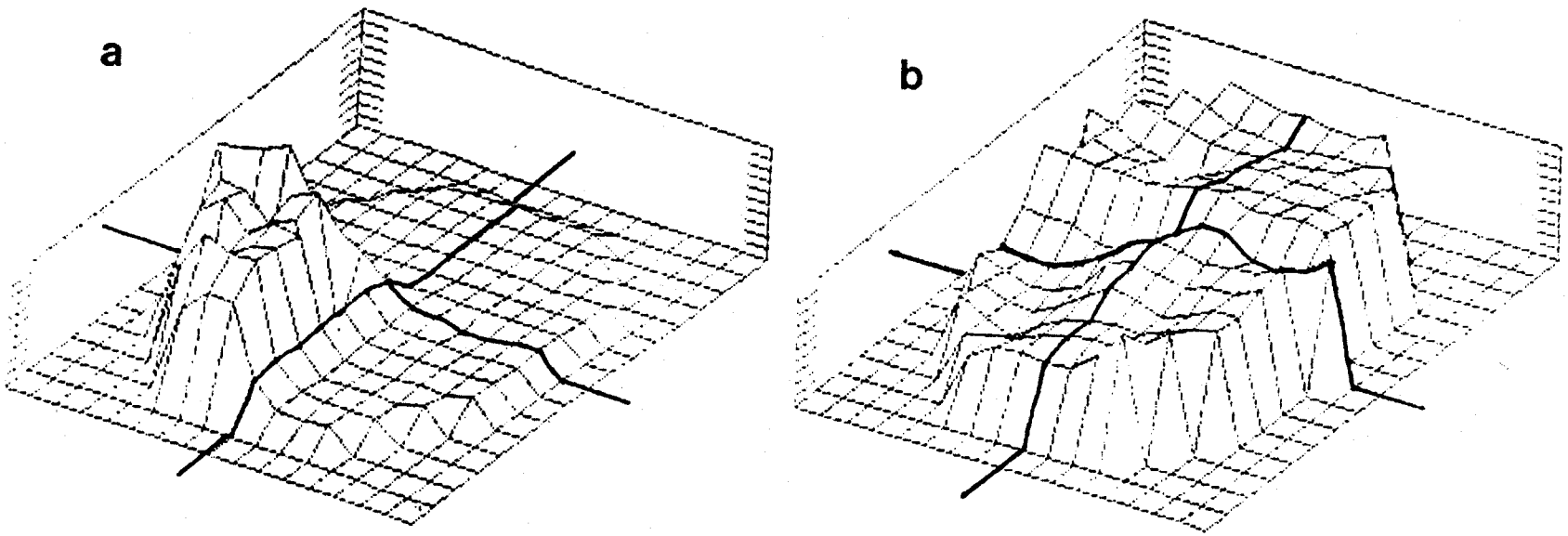

Fig.16 Map of recombination lifetime after 30 sec RTA treatment at condition shown in Fig.11, measured at **a** room temperature, and **b** 200°C.

the lifetimes were measured at 200°C, since at elevated temperature recombination and not generation effects are dominant. For metal implanted samples, the bulk lifetime initially slightly increases with temperature within low RTA temperature range (up to 400°C), most likely due to gettering properties of the dislocations. It then decreases within a middle temperature range, when implanted contaminants start to diffuse into semiconductor bulk. At the end, lifetime increases again after impurities are collected at the MD but this increase is not higher than the initial lifetime value. For the reference wafer, lifetime after initial increase decreases monotonically with RTA temperature and reaches the same value as for metal doped samples. It is most likely that lifetime in the bulk of the samples annealed at 1000°C is controlled not by metal contaminants but by defects introduced by the RTA process. The surface lifetime referred to electrical activity of MD decreases slowly with the RTA temperature up to 800°C. This is associated with a surface recombination velocity increase at the decorated dislocations. However, above 800°C the dislocation activity abruptly decreases again (surface lifetime increases). We believe that this effect is related to the creation of an electric field at the MD which repels minority carriers from the dislocation plane. Notice that, in order to explain this electrical behavior, the formation of n-n^+ (but not a p-n) junction around the dislocation has to be introduced. This is because the electric field associated with a p-n junction attracts minority carriers and increases the observed surface recombination velocity at the junction plane, while a low-high concentration junction repels minority carriers and decreases the "effective" surface recombination.

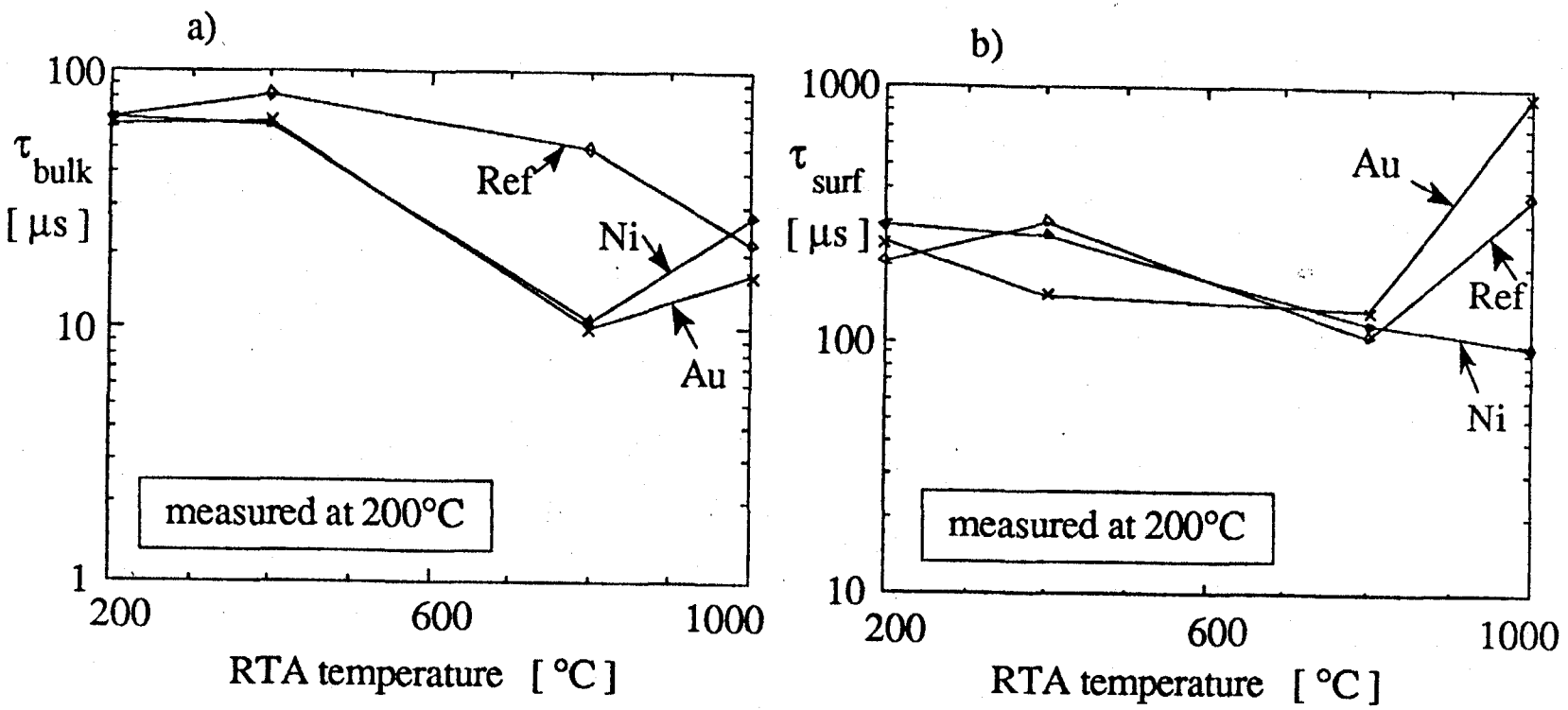

Fig.17 Influence of RTA temperature on **a** bulk and **b** surface component of lifetime measured at 200°C.

4 Energy Levels of Defects

The electrical properties of defects have been characterized using various methods such as a pulsed MOS capacitor method [34], a diode recovery method [35], a photoconductive decay method [36], a surface photovoltage method [37], and measurement of the diode leakage current [38]. From the material characterization point of view, a noncontact method which requires no specific sample preparation is desired since it is free from introducing additional defects or impurities. Recently, a new noncontact and nondestructive method for deep level measurement, laser/microwave deep level transient spectroscopy (LM-DLTS), has been reported [39]. Moreover, the energy levels related to metallic impurities in silicon obtained by this method have corresponded well to those obtained by a conventional DLTS method [40]. In this study, the LM-DLTS method is applied to characterize the energy levels due to crystal defects in heat treated CZ silicon wafers with different [Oi], [Cs], and thermal history during crystal growth.

4.1 Impact of Energy Level on EBIC/SEM Signal

Before discussing the experimental results on clean and decorated defects the important issue of the detection limit of the EBIC/SEM technique must be addressed since this technique is the one most often used to verify that a particular defect is an electrically active or inactive element. Assuming that energy levels can arise within the Si band gap from the lattice disturbance, one can expect that discrete levels will be associated with clean structural defects [41]. In this case the electrical activity should be correlated with the number of broken or disturbed bonds introduced by a specific defect. This approach is supported by the results of Pasemann et al.[2] who showed, for example, that 60° dissociated dislocations are more active than screw dislocations. The more important issue, we must consider, is where a defect energy level is situated within the band gap. According to the Shockley-Read-Hall theory [12], the probability of recombination is the highest for defects

occupying deep levels, i.e. close to the middle of band gap, and decreases significantly for shallower energy levels [42,43]. It is important to mention that the temperature dependence of the defect electrical activity depends strongly on the energy level position within the band gap [44,45]. In order to better understand this relationship the recombination lifetime of silicon was calculated using the SRH theory with defect energy level as a parameter. The results are presented in Fig. 18 for various levels starting from the 0.16 eV (shallow) up to 0.56eV (deep). The trap concentration was assumed to be $10^{13}/cm^3$ and capture cross section $2x10^{-15}/cm^2$. As expected, deep traps are the most active, thereby yielding the lowest lifetime values and their level of activity is practically temperature independent. Thus the EBIC signal for deep traps would be expected to remain the same for the temperature range investigated in this work. This observation has been made for gold diffused sample as well as for Ni precipitates for which the EBIC contrast practically does not vary within the investigated temperature range (300K to 120 K). On the other hand, shallow or mid-level traps are less active at high temperature yielding substantially higher lifetimes. According to data from Fig. 18, their activity increases strongly with decreasing temperature, allowing, for example, a 0.16eV energy level to reach the activity of a 0.56 eV level at 150K. A very similar behavior was observed for the Ni diffused sample. The non-decorated parts of misfit dislocations are barely visible at room temperature; however they become very active at low temperature, indicating that they occupy a shallower level in the band gap.

A significant change in EBIC contrast is observed for the same structure when imaged at 120 K, see Fig. 19a and b. All dislocations become very active at low temperature, approaching the activity of the Ni precipitates. Important to mention that the EBIC contrast did not change when the sample temperature was decreased to 120 K.

Analyzing the above experimental data, one can clearly confirm that the electrical activity of a dislocation is strongly correlated with the level of impurity introduced during processing since the activity increased for each contaminant as the sample annealing

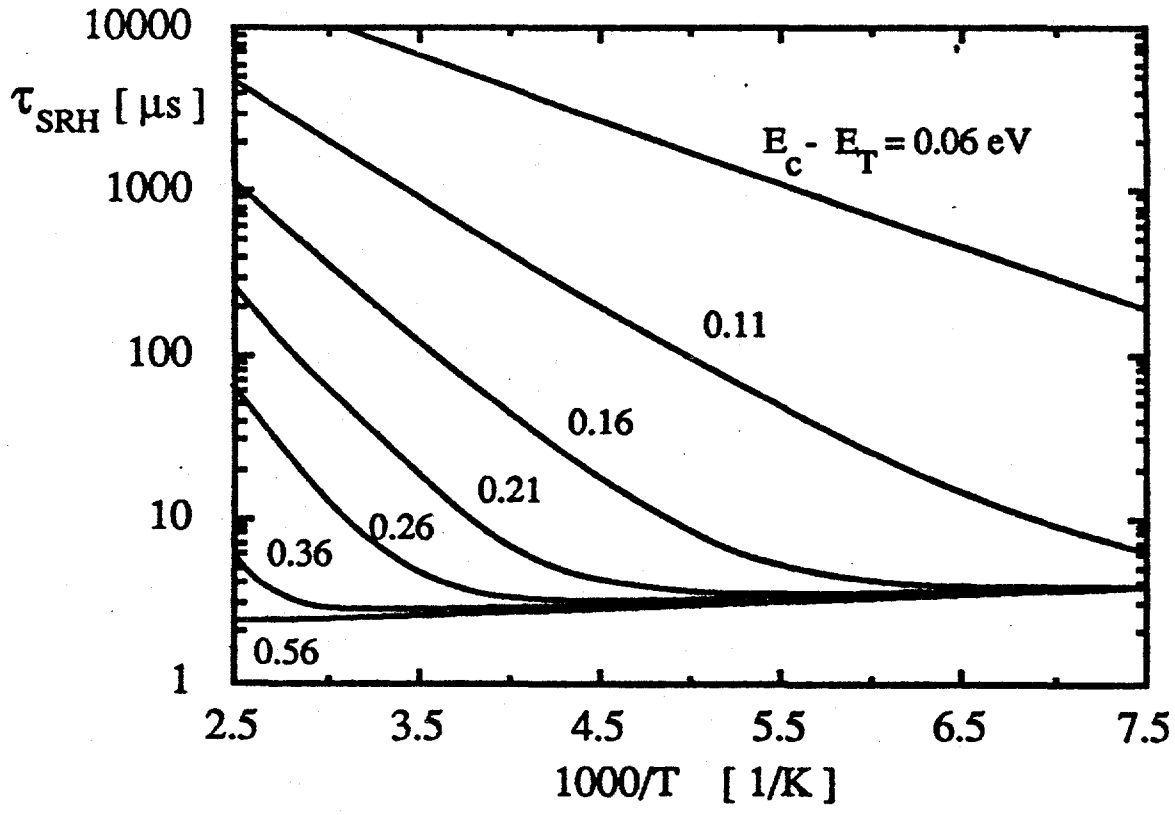

Fig. 18 Theoretical lifetime vs. temperature relationship with activation energy as a parameter.

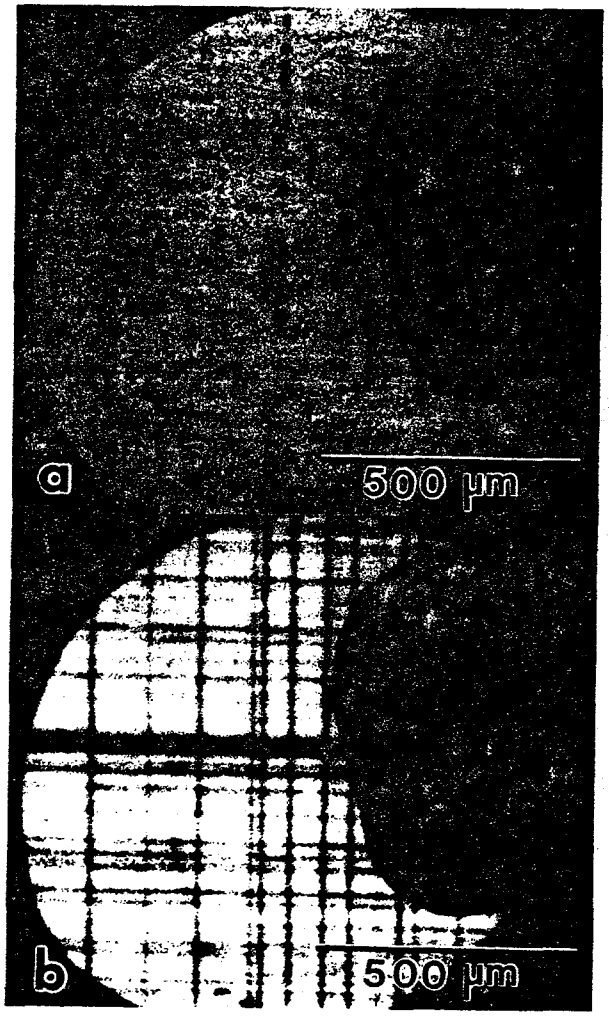

Fig. 19 EBIC/SEM image of heterostructure with misfit dislocations decorated with Ni at 1000°C obtained at **a** room temperature, and **b** at 120K.

temperature increased. It is, however,very difficult to state that clean dislocations are, in fact, electrically inactive simply because they are not visible in EBIC images. The different activity of various energy levels implies that a threshold may exist for the EBIC contrast since it is based on the recombination properties of defects [46]. Therefore, defects with a medium energy level may not be easily detectable. This also relates to the high purity interfacial misfit dislocations investigated in this work. We believe that these dislocations may indeed introduce shallow levels to the band gap, whose electrical activity at room temperature is below the EBIC detection limits. If additional deep levels arise from impurity decoration, then the same structural defect could be clearly identified in EBIC images taken at room temperature as a defect-impurity complex. This is in agreement with the observations of Schröter et al. [47], who noted that only defects with states deeper than roughly 0.3 eV contribute to an EBIC signal at room temperature. One should remember also that the concentration of traps introduced by the complex, as well as their capture cross-section must also be taken into account while discussing recombination properties of defects.

4.2 Energy Level of Defects Measured by LM-DLTS System

Silicon samples used for this study were prepared from six CZ silicon ingots (n<100>, 150 mm-diam, 20~30 ohm-cm) with different oxygen and carbon concentrations. The concentrations of interstitial oxygen ([Oi]) and substitutional carbon ([Cs]) were measured with FT-IR according to the ASTM procedures [48,49]. The initial oxygen concentration ($[Oi]_O$) was controlled to be in three levels, i.e., L(low), M(middle), and H(high), ranging 13.3~16.4x10^{17} cm^{-3}, while the initial carbon concentration ($[Cs]_O$) was in two levels, i.e., L(low: $\leq$1x10^{15} cm^{-3}) and H(high: ~1x10^{16} cm^{-3}), without and with doping carbon powders into the silicon melt, respectively. To achieve identical thermal history during crystal growth for all the ingots, they were grown about 600 mm in body length under the same growth conditions except for [Oi] and [Cs] control. Wafers of

650 mm-thick and slugs of 2 mm-thick were cut from the identical position of the ingots, i.e., 200~300 mm from the seed end. All the wafers were single-side polished and followed by cleaning with standard processes, while slugs were chemically etched with an HNO_3-HF acid solution to be finished with mirror surfaces. The energy levels in those wafers were measured with the LM-DLTS method using LIFETECH-88® (SEMITEX Co., LTD.) after heat treatments under several conditions. Before and after each annealing step, [Oi] and [Cs] were monitored using slugs which were heat treated under the same conditions as those for wafers. The [Oi] and [Cs] of samples used in this study are listed in Table I. The defect morphology in wafers after heat treatments were characterized with transmission electron microscopy (TEM). In this study, the annealing ambient was N_2 (95%) and O_2 (5%) mixed gas, and push/pull rate was 20 cm/min without ramp-up and ramp-down.

(A) Oxygen and carbon related crystal defects

After iso-chronal annealing at different temperatures (750 °C / 64h or 1000 °C / 64h), two different energy levels around 0.20 and 0.25 eV were observed. For example, the Arrhenius plots for wafers E(H-L); high Oi - low Cs, and F(H-H); high Oi - high Cs, are shown in Fig.20. After 1000 °C / 64h annealing, both the wafers showed an energy level around 0.20 eV. An energy level around 0.25 eV was observed in wafer F(H-H) after 750 °C annealing, but not in wafer E(H-L) subjected to the same annealing. The energy levels observed in six wafers after the iso-chronal annealing are summarized in Table 2. The wafers have the identical thermal history, but are different in $[Oi]_o$ and $[Cs]_o$. The energy level around 0.25 eV was observed only in carbon doped wafers which were annealed at 750 °C, but not at 1000 °C.

The possible causes for carrier trap generation are expected to be; (i) the interface states between thermal oxide and silicon substrate, (ii) contamination of metallic impurities, and (iii) bulk crystallographic defects. To investigate the effective lifetime (τ_{eff}) of these

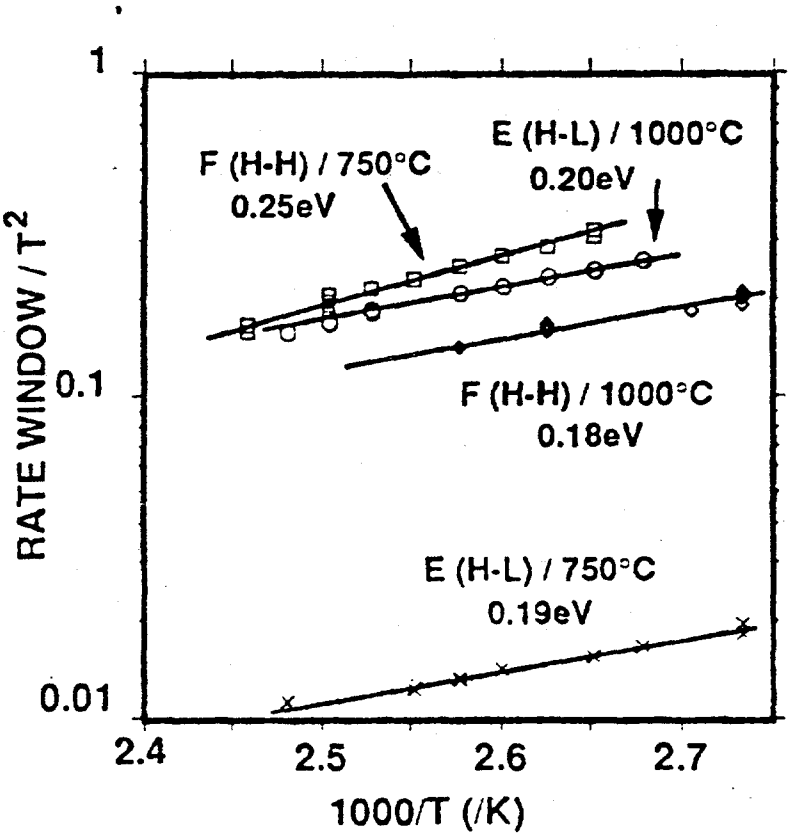

Fig.20 Arrhenius plots for the recombination centers, which were obtained for wafers E(H-L) and F(H-H) after isochronal annealings (750°C/64h or 1000°/64h)

Table 2 Samples used in this study are listed with oxygen concentration ([Oi]o), oxygen reduction (Δ[Oi]) and activation energy (Ea) obtained after isochronal annealing for 64h at 750 and 1000°C.

WAFER	$[Oi]_0$	1000°C / 20min.		750°C / 64h		1000°C / 64h	
$[Oi]_0$-$[Cs]_0$*	xE17/cc	Δ[Oi]	Ea(eV)	Δ[Oi]	Ea(eV)	Δ[Oi]	Ea(eV)
A (L-L)	13.8	0.0	NO	0.2	0.19	0.4	0.19
B (L-H)	13.3	0.0	NO	0.7	0.26	0.3	0.20
C (M-L)	14.7	0.0	NO	0.0	0.17	0.5	0.17
D (M-H)	14.8	0.0	NO	5.1	0.25	7.2	0.17
E (H-L)	16.3	0.0	NO	0.1	0.19	4.5	0.20
F (H-H)	16.4	0.0	NO	14.7	0.25	14.8	0.18

* $L \leq 1 \times 10^{15} cm^{-3}$, $H = 0.8 \sim 1.2 \times 10^{16} cm^{-3}$ $(k = 1.0 \times 10^{17} cm^{-2})$

wafers after the crystal growth, and the trap levels resulted from the interface between thermal oxide and silicon substrate, another set of samples from each ingot were prepared by oxidizing at 1000 °C for 20 min in O_2 (50%) and N_2 (50%) mixed gas. The t_{eff} of these wafers were over 2 msec. No trap level was observed after this oxidation in all the wafers. Therefore, it can be concluded that the wafers used in this study were not contaminated with metallic impurities, and contained no crystallographic defects which can be identified before the iso-chronal annealing. This result means that the trap levels observed after the iso-chronal annealings are not due to surface or interface states, but due to bulk crystallographic defects generated during annealing process.

Figures 21a-d show TEM pictures for wafers E(H-L) and F(H-H) after annealing at 750 and 1000 °C for 64h. The results did not show any significant effect of carbon on crystallographic defects generated. After 750 °C annealing, {100} square platelet oxygen precipitates were observed in both wafers. The {100} square platelet associated with punched-out dislocation loops and precipitate-dislocation complexes were observed in both wafers after 1000 °C annealing.

The recombination properties of crystal defects in annealed CZ silicon were reported by Hwang et al. [50], and they investigated the efficiency of defect morphology on lifetime degradation. It was found that oxygen precipitates are mainly responsible for lifetime degradation, and the recombination process at oxygen precipitates take place through the interface between the precipitates and the matrix silicon crystal. Considering their result, one may conclude that the two trap levels obtained in the present experiment are due to {100} square platelet oxygen precipitates and invisible defects in Cs-rich samples, and the difference in energy level is caused by the difference in their electrical and/or chemical properties.

The IR absorption spectra for as-grown sample F(H-H) and those subjected to heat treatments at 750 and 1000 °C are shown in Fig. 22. These spectra were obtained by subtracting the IR spectrum of an FZ reference sample. The peaks at 515 cm^{-1} (n_{O2}) and

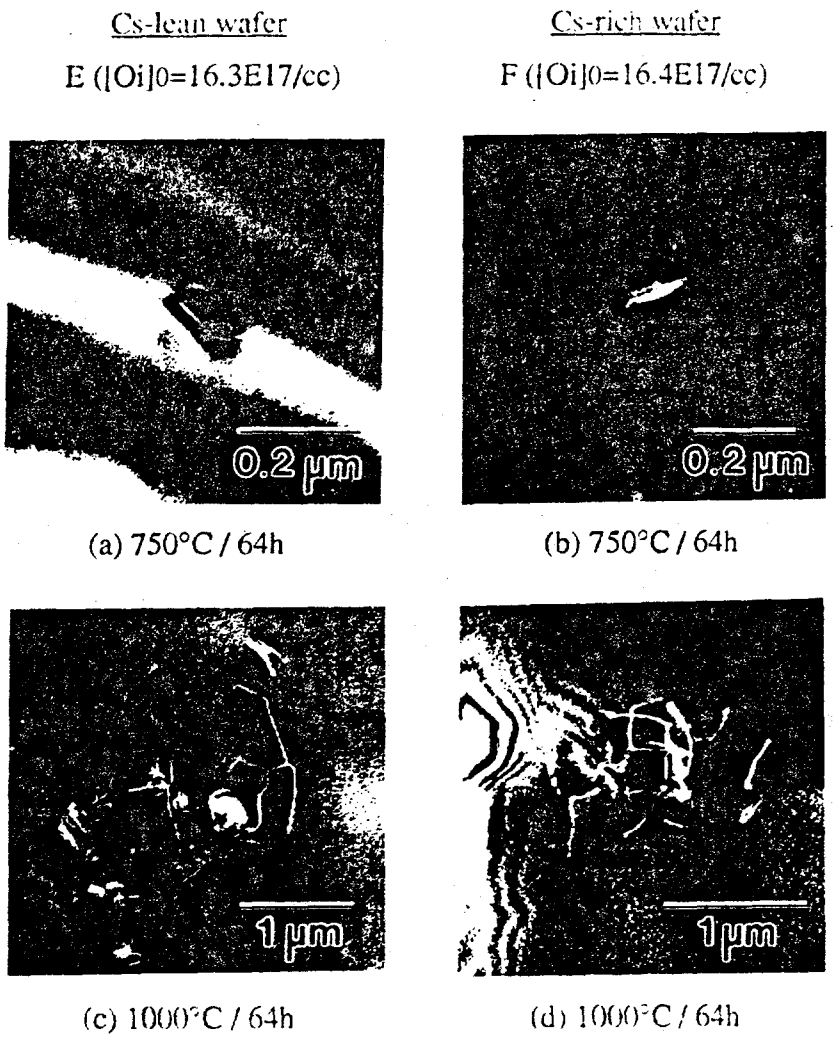

Fig.21 Typical defects in wafers E(H-L) and F(H-H) after isochronal annealings. **a** and **b**: a {100} platelet oxygen precipitate, and **c** and **d**: precipitate-dislocation complexes for for wafers E(H-L) and F(H-H), respectively

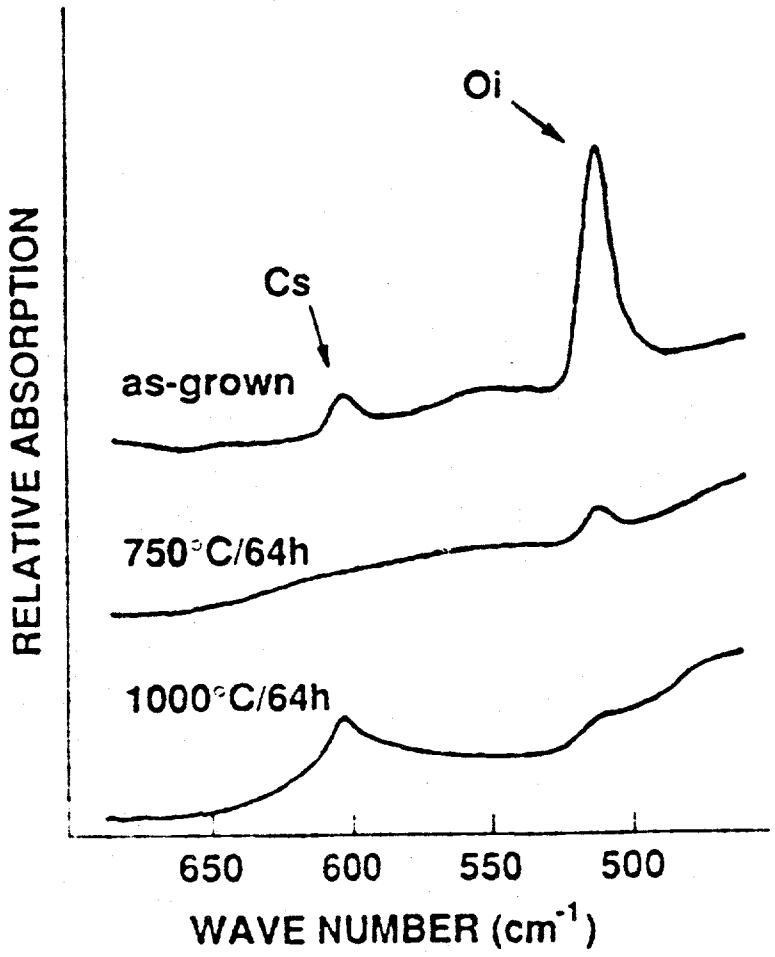

Fig.22 IRE absorption spectra for sample F(H-H) after isochronal annealing for 64h at 750°C and 1000°C are shown with that of an as-grown sample.

607 cm^{-1} (n_C) are due to Oi [51] and Cs [52], respectively. As shown in this figure, the n_{O2} peak decreased in both samples annealed at 750 and 1000 °C showing oxygen precipitation. However, the n_C peak disappeared in the sample annealed at 750 °C, while remained in the sample annealed at 1000 °C. The origin of a broad band around Cs peak in the sample annealed at 1000 °C might be crystallographic defects generated in this sample. The result mentioned above means that Cs precipitated during annealing at 750 °C, but not at 1000 °C.

Shimura reported [53] the enhancement effect of carbon on oxygen precipitation in CZ silicon. He concluded that there is a critical temperature Tc (800 °C<Tc<850 °C) to distinguish the mechanism in which carbon enhances oxygen precipitation; that is, carbon directly provides heterogeneous nucleation sites ([Ci-Oi]C(3) centers) for oxygen precipitation at temperatures lower than Tc, while carbon plays a catalytic role at temperatures higher than Tc. Considering the above mentioned results, it is supposed that the 0.25 eV level is due to carbon-oxygen clusters, called the complex "perturbed C(3) center", which were generated during the annealing lower than Tc (750 °C).

(B) Oxygen related microdefects

Intrinsic gettering (IG) [54,55] has been widely used in ULSI processes to improve device performance and yield. Usually, three-step annealing at high-low-middle temperatures are performed to out-diffuse oxygen impurities for forming a denuded zone, nucleation for defect generation, and growth of crystal defects, respectively. Figure 23 shows the change in [Oi] for wafers E(H-L) and F(H-H) after each step (1st: 1100 °C / 4h, 2nd: 750 °C / 64h, and 3rd: 1000 °C / 16h). Wafers E(H-L) and F(H-H) have the same initial [Oi] (16.5×10^{17} cm^{-3}) and identical thermal history during crystal growth, but have different in $[Cs]_0$ ($[Cs]_E \leq 1.0 \times 10^{15}$ cm^{-3} and $[Cs]_F = 1.0 \times 10^{16}$ cm^{-3}). No significant reduction [Oi] (i.e., D[Oi]) was observed in both wafers after the first and second steps. After the third step, however, wafer F(H-H) shows much greater D[Oi] in contrast with wafer E(H-L). This fact implies that more nuclei for oxygen precipitates were generated in

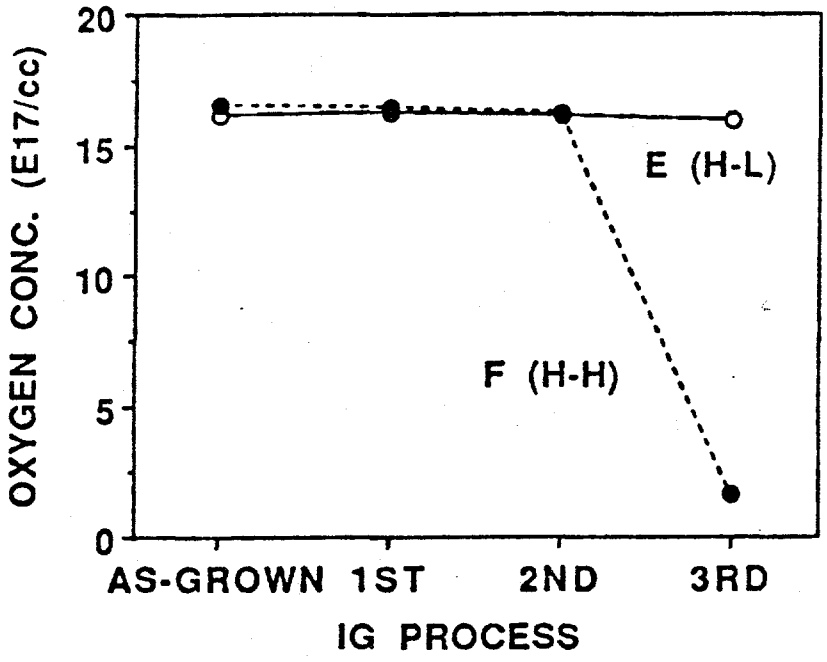

Fig.23 Oxygen concentration in wafers E(H-L) and F(H-H) after each step of a three step IG process simulation (1st: 1100°C/4h, 2nd: 750°C/64h, and 3rd: 1000°C/16h)

wafer F(H-H) more than in wafer E(H-L) during the second step and the precipitation was enhanced during the third step because of higher [Cs] in wafer F(H-H). Figures 24a and b show the DLTS signals after the second step for samples E(H-L) and F(H-H). No energy level was observed in wafer E(H-L); while, wafer F(H-H) clearly showed an energy level at 0.28 eV although significant oxygen precipitation was not observed with FT-IR measurement. These experimental data suggest that the energy level is due to the nuclei for oxygen precipitates and/or oxygen related microdefects in wafer F(H-H).

(C) Effect of oxygen concentration on trap generation

The concentration of oxygen is one of the factors which most dominantly affect oxygen precipitation in silicon [56]. The DLTS signals for F(H-H) and B(L-H) are shown in Figs. 5(b) and (c). These wafers contain different initial [Oi], i. e., 16.5 and 13.5×10^{17} cm^{-3}, respectively, but identical $[Cs]_0$ and thermal history. These were annealed with a two-step process (1100 °C / 4h + 750 °C / 64h). As it was mentioned in section (B), no significant D[Oi] was observed not only in wafer F(H-H) but also in wafer B(L-H). However, the signal decrement (DV) in wafer F(H-H) clearly shows the temperature (Tm) which gives a peak of DV at a particular rate window, and the resulting Arrhenius plot gives an energy level at 0.28 eV. On the other hand, in wafer B(L-H), the dependence of DV on temperature is weak although this wafer contains high [Cs] to act as nuclei for oxygen precipitates. Therefore, it is difficult to obtain a trap level by designating Tm. Considering these results, one may find that the density of trap levels generated during annealing increases with initial [Oi]. This result corresponds with the enhancement effect of oxygen supersaturation on the oxygen precipitation.

(D) Effect of high temperature pre-annealing

It is well known that a high temperature annealing retards oxygen precipitation during subsequent annealing. Figures 24a and d show the DLTS signals from two E(H-L) wafers after 1100 °C / 4h + 750 °C / 64h and 750 °C / 64h iso-chronal annealing,

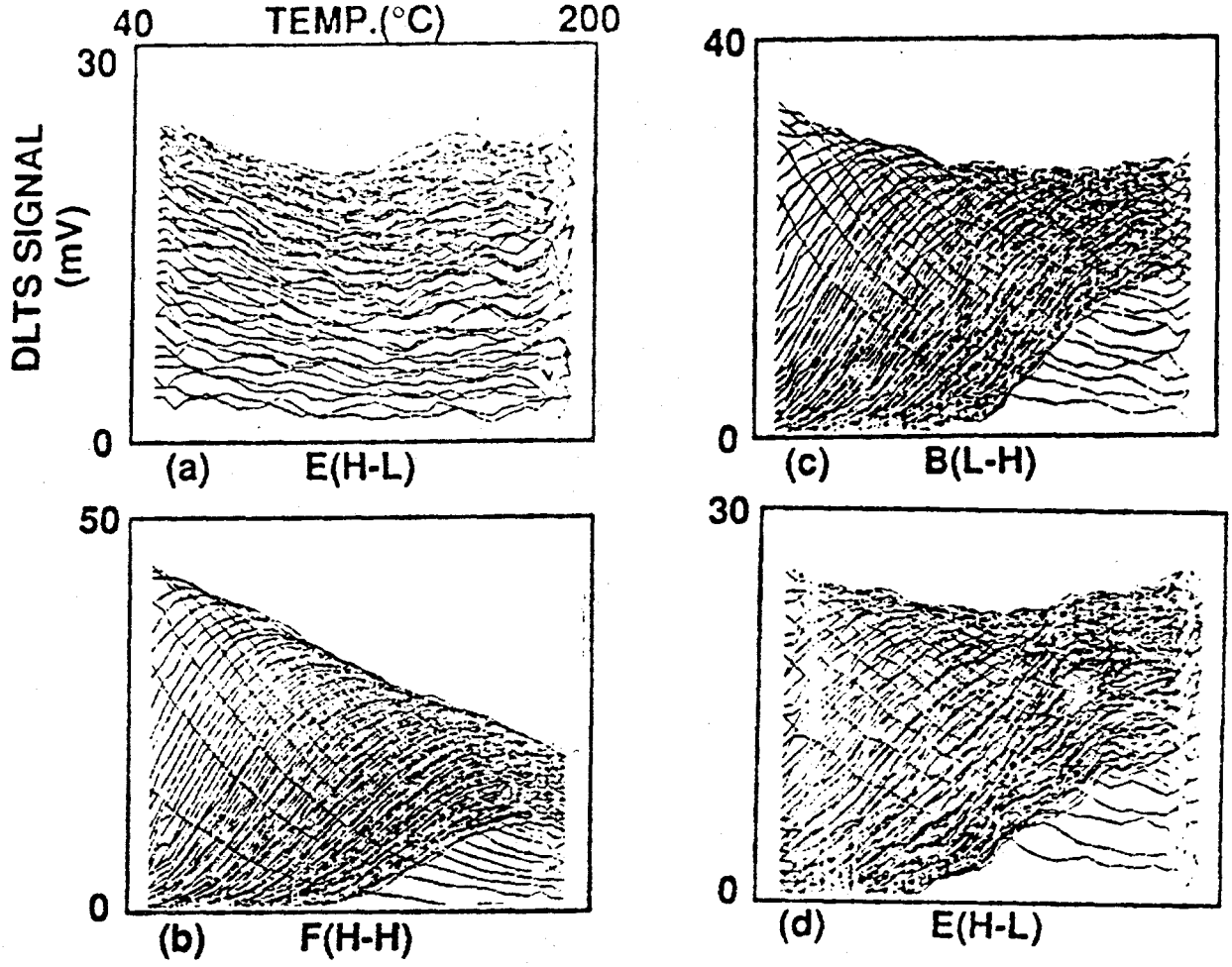

Fig.24 LM-DLTS signals obtained for six wafers after an iso-chronal annealing (750°C/64h) a wafer E(H-L):1100°C/4h+750°C/64h, b wafer F(H-H):1100°C/4h+750°C/64h, c wafer B(L-H):1100°C/4h+750°C/64h, and wafer E(H-L): 750°C/64h.

respectively. Although both wafers showed no significant D[Oi] after the annealing as shown in Fig. 23 and Table 2, wafer E, Fig. 24d, manifests an energy level at 0.19 eV. As mentioned in section (A), this trap level is due to interface state between oxygen precipitates and matrix silicon crystal. However, in wafer E, Fig. 24a, the dependence of DV on temperature is weak compared with that of wafer E, Fig. 24d, as a result of a low trap density in wafer E, Fig. 24a. It is therefore difficult to designate an energy level for wafer E subjected to a high-temperature pre-annealing at 1100 °C. This means that wafer E, Fig. 24a contains low trap levels because of its low density of oxygen precipitates. This result supports that the retardation effect of high temperature pre-annealing on oxygen precipitation is due to the lack of microclusters which can be nucleation centers for oxygen precipitates [57].

(E) Effect of thermal history during crystal growth

Thermal history during crystal growth strongly affects the rate of oxygen precipitation during heat treatment. In general, a sample prepared from a bottom portion in one ingot shows much less D[Oi] by annealing than samples from other portions. This fact has been considered that the former contains much less nuclei for oxygen precipitation than the latter because of its rapid cooling rate, which also results in a short thermal history, in a crystal puller.

Figure 25 shows the Arrhenius plots for two wafers after iso-chronal annealing at 750 °C for 64h. These wafers have almost same initial [Oi] (13.8×10^{17} cm^{-3} for A(M:middle) and 13.2×10^{17} cm^{-3} for A(B:bottom)), but different thermal history in one ingot; namely, A(M:middle) and A(B:bottom) were prepared from 200~300 mm and 500~600 mm from the seed end, respectively. In both these samples, a trap level at 0.19 eV was obtained. After the iso-chronal annealing, D[Oi] was negligibly small for both wafers. Nevertheless, the total cross section of the trap level is much higher in wafer A(M:middle) than in wafer A(B:bottom); which suggests that a low density of precipitates were generated in wafer

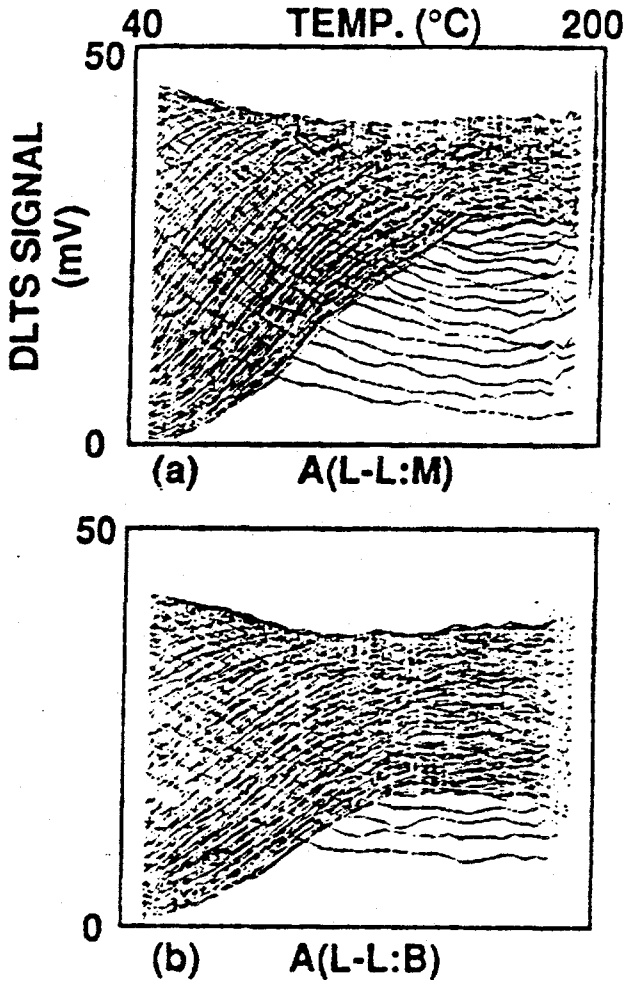

Fig.25 LM-DLTS signals obtained for a wafer A(L-L:M) and b wafer A(L-L:B) after 750°C iso-chronal annealing for 64 h. These were prepared from middle (M) and bottom (B) portions in a ingot.

A(B:bottom). This result supports previous observations on the effect of thermal history on oxygen precipitation [58,59].

RECOMMENDATION

The above report describes recent achievements at NCSU in nondestructive analysis of the minority carrier lifetime parameter in Si/Si-Ge materials, the evaluation of clean and impurity decorated defect structures in these materials and the electrical activity of such defects by LM-DLTS, EBIC/SEM and other techniques. All of these studies are directed toward making technological contributions of real economic value in the field of defect engineering for photovoltaic materials .

However, extensive work remains in acquiring the detailed scientific knowledge to facilitate process innovations to control the electrical activity of structural defects present in crystalline Si wafer, dendritic web and EFG ribbon materials. We are now in a good position to design and employ a complement of nondestructive methods for defect characterization based on whole wafer imaging with X-Ray (XRT) and Scattering Topography (LST) as well as further development of LM-DLTS techniques. It is considered here that LM-DLTS results must be comparison tested against our own in-house conventional depletion layer capacitance DLTS system now under development. This will allow us to give special consideration in evaluating our LM-DLTS techniques when investigating certain unique physical properties of clean/decorated structural defects such as the formation of depletion layers around misfit dislocations which might effect energy level and minority carrier lifetime determination. The recently developed LST technique will be used for mapping the fine structural and morphological details. The result of this study correlating electrical/defect properties will solve a basic problem which exists with conventional space charge relaxation techniques, i.e. the need for processing to contact the sample surface will be eliminated. Representative photovoltaic substrates in the as-grown, gettered, passivated and device fabrication stage will then be mapped over areas up to 5 inches in diameter.

Also planned is a study of the electrical activity of process induced and passivated defects. The objective of this work is to investigate a variety of post-growth processes which are likely to decrease the electrical activity of defects and to improve the performance of crystalline silicon photovoltaic materials. Our main interest will be focused on defect passivation using hydrogen implantation and diffusion, although issues related to the electrical behavior of "clean" and decorated dislocations will be explored. The overall objective will be:

- to determine the diffusion coefficients and gettering mechanism of hydrogen in different crystalline materials containing a variety of defect types,
- to correlate the electronic hydrogen passivation with the chemical / structural nature of the different impurity-defect complexes,
- to develop less destructive procedures for hydrogenation.

The structural and chemical studies will be focused on determining the type of impurity, the size of the impurity/defect complexes and the level of associated damage. Of particular interest will be merging EBIC/SEM and scanning DLTS for the temperature dependence of the defect electrical activity and the temperature dependence of carrier lifetime and diffusion length, parameters which reflect global properties of crystalline silicon. Practical data on hydrogen diffusivities in a variety of substrates of interest to SERI will be generated and modeled.

RELATED PUBLICATIONS

1. *"Bulk and surface component of recombination lifetime based on a two-laser microwave reflection technique"*, J. Appl. Phys. **69**, 6495 (1991), A. Buczkowski, Z. J. Radzimski, G. A. Rozgonyi, and F. Shimura

2. *"Electrical Activity of Dislocations: Prospect for Practical Utilization"*, To be published to Appl. Physics A (1991), Z. J. Radzimski, T-Q. Zhou, A. Buczkowski, and G. A. Rozgonyi

3. *"Noncontact Analysis for Si (1%Ge)/Si Heterostructure with Laser/ Microwave and X-ray Imaging Techniques"*, to be published in **Defects in Silicon II**, edited by W.M. Bullis, U. Gösele and F. Shimura, ECS Proc. Vol.**91**, (The Electrochemical Society, Pennington, NJ, 1991), A. Buczkowski, Y. Kirino, T-Q. Zhou, Z. J. Radzimski, D. Finn, L. Hellwig, J. Rossi, G. A. Rozgonyi, and F. Shimura

4. *"EBIC Contrast of Clean, Decorated and Deuterium Passivated Si(Ge) Epitaxial Misfit Dislocations"*, ibid, T-Q. Zhou, A. Buczkowski, Z.J. Radzimski, C.H. Seager, J. Panitz and G.A. Rozgonyi

5. *"LM-DLTS Measurements for CZ Silicon Wafers with Different [Oi], [Cs], and Thermal History"*, ibid, K. Katayama and F. Shimura

6. *"The Gettering and Electrical Activity of Metallic Impurities in Epitaxial Si/Si(Ge) During Rapid Thermal Annealing"*, to be published in **Rapid Thermal and Integrated Processing,** edited by J. Gelpey, M. Green J. Wortman, and R. Singh (MRS, Pittsburgh, PA 1991), MRS Proc. Vol. **224**, T-Q. Zhou, A. Buczkowski, Z.J. Radzimski, and G.A. Rozgonyi

REFERENCES

1. C. Donolato, Phys. Stat. Sol. (a), **66**, 445 (1981)
2. L. Pasemann, H. Blumtritt and R. Gleichmann, Phys. Stat. Sol. (a), **70**, 197 (1982).
3. C. H. Dimitriadis, Solid State Electronics, **26**, 633 (1983)
4. A. Jakubowicz, J. Appl. Phys., **57**, 1194 (1985)
5. A. Kittler, Solid State Phenomena, **6 & 7**, 367, (1989)
6. D. B. Holt, E. Napchan and C. E. Norman, Inst. Phys. Conf. Ser. **104**, 205 (1989)
7. A. Ourmazd and G. Booker, Phys. Stat. Sol. (a), **55**, 771 (1979).
8. H. Blumtritt, R. Gleichmann, J. Heydenreich and H Johansen, Phys. Stat. Sol. **55**, 611 (1979)
9. L. Castellani, P. Gondi, C. Patuelli and R. Berti, Phys. Stat. Sol. (a), **69**, 677 (1982)
10. D.M. Lee, J.B. Posthill, F. Shimura and G.A. Rozgonyi, Appl. Phys. Lett. 53, 370 (1988)
11. D.M. Lee, D.M. Maher, F. Shimura, and G.A. Rozgonyi, in Semiconductor Silicon 1990, edited by H.R. Huff, K.G. Barraclough and J. Chikawa (The Electrochemical Society, Pennington, NJ, 1990), p.638
12. D.K. Schroder, *Semiconductor Material And Device Characterization*, John Wiley & Sons, New York, 359-448, (1990).
13. J. W. Orton and P. Blood, *The Electrical Characterization of Semiconductor: Measurement of Minority Carrier Properties*, Academic Press, San Diego, 1990
14. Y. Mada, Japan. J. Appl. Phys. **18**, 2171 (1979).
15. F. Shimura, T. Okui and T. Kusama, J. Appl. Phys. **67**, 7168 (1990).
16. T. Warabisako, T. Saitoh, T. Motooka and T. Tokuyama, Japan. J. Appl. Phys. **Supl.22-1**, 557 (1982).
17. J. Waldmeyer, J. Appl. Phys. **63**, 1977 (1988).
18. T. Tiedje, J. I. Haberman, R. W. Francis, and A. K. Ghosh, J. Appl. Phys. **54**, 2499 (1983).
19. U. Lehmann and H. Foll, J. Electrochem. Soc. **135**, 2831 (1988).
20. K. L. Luke and L. J. Cheng, J. Appl. Phys. **61**, 2282 (1987).
21. Y. Ogita, *Extended Abstracts*, **90-1**, The Electrochemical Society Meeting, Montreal, Canada, May 1990, 702 (1990).

22 E. S. Nartowitz and A. M. Goodman, J. Electrochem. Soc. **132**, 2992 (1985).

23 Y. Kirino, A. Buczkowski, Z. Radzimski, G. Rozgonyi and F. Shimura, Appl. Phys. Lett., **57**, 2832 (1990)

24 F. Shimura, T.Okui and T.Kusama, J. Appl. Phys. **67**, 7168 (1990).

25 Y. Kirino, A. Buczkowski, Z. Radzimski, G. A. Rozgonyi and F. Shimura , Appl. Phys. Lett. **57**, 2832 (1990).

26 F. Shimura, in Proc. Japan Semicon. Tech. Forum, VI-3, 1989 (Japanese).

27 A. Buczkowski, Z. Radzimski, Y.Kirino, F. Shimura and G. Rozgonyi, MRS Symposium Proc., edited by P. Bristowe, J. Epperson, J. Griffith and Z. Liliental-Weber (MRS Pittsburgh, Pennsylvania, 1991), **209**, 567

28 D. Lee, D. Maher, F. Shimura and G. Rozgonyi, p. 639 *in Semiconductor Silicon 1990*, edited by H. Huff K. Barraclough and J. Chikawa (The Electrochemical Society, Pennington, NJ, 1990).

29 Z. Radzimski, T. Zhou, A. Buczkowski and G. Rozgonyi, *Electrical Activity Of Dislocations: Prospect For Practical Utilization*, to be published in J. Physics (GB).

30 A. S. M. Salih, H. J. Kim, R. F. Davis and G. A. Rozgonyi, Appl. Phys. Lett. **46**, 419 (1985).

31 A. Buczkowski, Z. Radzimski, G. Rozgonyi and F. Shimura, J. Appl. Phys. **69**, 6495, 1991.

32 K. L. Luke and L. J. Cheng, J. Appl. Phys. **61**, 2282 (1987).

33 J. W. Orton and P. Blood, *Electrical Characterization of Semiconductors: Measurements of Minority Carrier Properties* (Academic, San Diego, 1990).

34 D. K. Schroder, J. D. Whitfield, and C. J. Varker, IEEE Trans.Electron Devices ED-31 463 (1984).

35 C. J. Varker, J. D. Whitfield, and P. Fejes, Material Research Society Symposium Proceedings, Vol.14, edited by S.Mahajan and J.W.Corbett (North-Holland, NY,1983), p.187.

36 M. Miyagi, K. Wada, J. Osaka, and N. Inoue, Appl. Phys. Lett. 40 719 (1982).

37 D. K. Schroder, J. M. Hwang, J. S. Kang, A. M. Goodman, and B. L. Sopori, in *"VLSI Science and Technology 85"*, edited by W. M. Bullis and S. Broydo (Electrochemical Society, Princeton, NJ,1985), p.419.

38 S. N. Chakravarti, P. L. Garbarino, and K. Murty, Appl. Phys. Lett. 40 581 (1982).

39 Y. Kirino, A. Buczkowski, Z. J. Radzimski, and F. Shimura: The Electrochemical Society Meeting Extended Abstracts: Vol. 90-2, p. 585 (1990).

40 Y. Kirino, A. Buczkowski, Z. J. Radzimski, G. A. Rozgonyi, and F. Shimura, Appl. Phys. Lett. 57 2832 (1990).

41 H. J. Queisser, MRS Symp. Proc., **14**, 323 (1983).

42 L. C. Kimmerling, H. J. Leamy and J. R. Patel, Appl. Phys. Lett. **30**, 217, (1977).

43 M. Kolbe, O. Hollricher, H. Gottschalk and H. Alexander, Inst. Phys. Conf. Ser. No. **100**, 725 (1989).

44 L. J. Cheng, MRS Symp. Proc., **36**, 323 (1985).

45 Z. J. Radzimski, A. Buczkowski and G. A. Rozgonyi, (1990), ECS Proc. Vol. 90-15, 436.

46 A. Kittler and W. Seifer, Phys. Stat. Sol. (a), **66**, 573 (1981).

47 W. Schröter, I. Queisser and J. Kronewitz, Inst. Phys. Conf. Ser. No. **100**, 75 (1989).

48 ASTM F121, Ann. Book ASTM Stand. (1976) p. 518.

49 ASTM F123, Ann. Book ASTM Stand. (1984) p. 245.

50 J. M. Hwang and D. K. Schroder, J. Appl. Phys. 59 2476 (1986).

51 H. J. Hrostowski and R. H. Kaiser, Phys. Rev. 107 966 (1957).

52 R. C. Newman and J. B. Wills, J. Phys. Chem. Solids 26 373 (1965).

53 F. Shimura, J. Appl. Phys. 59 3251 (1986).

54 G. A. Rozgonyi, R. P. Deysher, and C. W. Pearce, J. Electrochem. Soc. 123 1910 (1976).

55 T. Y. Tan, E. E. Gardner, and W. T. Tice, Appl. Phys. Lett. 30 175 (1977).

56 F. Shimura and H. Tsuya, J. Electrochem. Soc. 129 1062 (1982).

57 F. Shimura, H. Tsuya, and T. Kawamura, Appl. Phys. Lett. 37 483 (1980).

58 H. Tsuya, F. Shimura, K. Ogawa, and T. Kawamura, J. Electrochem. Soc. 129 374 (1982).

59 G. Fraundorf, P. Fraundorf, R. A. Craven, R. A. Frederick, J. W. Moody, and R. W. Shaw, J. Electrochem. Soc. 132 1701 (1985).

Document Control Page	1. SERI Report No. SERI/TP-214-4503	2. NTIS Accession No. DE92001172	3. Recipient's Accession No.

4. Title and Subtitle
The Effectiveness and Stability of Impurity/Defect Interactions and Their Impact on Minority Carrier Lifetime

5. Publication Date
December 1991

6.

7. Author(s)
G. A. Rozgonyi, F. Shimura, A. Buczkowski, T.-Q. Zhon

8. Performing Organization Rept. No.

9. Performing Organization Name and Address
North Carolina State University
Raleigh, North Carolina 27695

10. Project/Task/Work Unit No.
PV121101

11. Contract (C) or Grant (G) No.
(C) XL-8-18097-2
(G)

12. Sponsoring Organization Name and Address
National Renewable Energy Laboratory
1617 Cole Blvd.
Golden, Colorado 80401-3393

13. Type of Report & Period Covered
Technical Report

14.

15. Supplementary Notes
NREL Technical Monitor: B. Sopori, (303) 231-1383

16. Abstract (Limit: 200 words)
This report covers the investigation and understanding of electrical activity of "clean" and metallic impurity decorated defects. A heterostructure containing a controlled number of deliberately introduced misfit dislocations is used as a model system to simulate a variety of defect/impurity interactions in photovoltaic materials. In addition, a noncontact laser/microwave deep-level transient spectroscopy technique is applied to characterize the minority carrier lifetime and determine the energy levels of defects.

17. Document Analysis
a. Descriptors
Photovoltaics ; minority carriers ; manufacturing ; defect/impurity interactions ; solar cells

b. Identifiers/Open-Ended Terms

c. UC Categories
270

18. Availability Statement
National Technical Information Service
U.S. Department of Commerce
5285 Port Royal Road
Springfield, VA 22161

19. No. of Pages
63

20. Price
A04

Form No. 0069E (6-30-87)